Analysis, Validation, and Improvement of High-Resolution Wind Estimates from the Advanced Scatterometer (ASCAT)

Jeffrey Richard Blodgett

A thesis submitted to the faculty of
Brigham Young University
in partial fulfillment of the requirements for the degree of

Master of Science

David G. Long, Chair
Dah Jye Lee
Karl F. Warnick

Department of Electrical and Computer Engineering, BYU

Brigham Young University

December 2014

ABSTRACT

Analysis, Validation, and Improvement of High-Resolution Wind Estimates from the Advanced Scatterometer (ASCAT)

Jeffrey Richard Blodgett
Department of Electrical and Computer Engineering, BYU
Master of Science

The standard L2B ocean wind product from the Advanced Scatterometer (ASCAT) is retrieved as a 25 km product on a 12.5 km grid. Ultra-high resolution (UHR) processing allows ASCAT wind retrieval on a high-resolution 1.25 km grid. Ideally, such a high-resolution sample grid provides wind information down to a 2.5 km scale, allowing better analysis of winds with high spatial variability such as those in near-coastal regions and storms. Though the wind field is sampled on a finer grid, the actual data resolution needs to be validated.

This thesis provides an analysis and validation of ASCAT UHR wind estimates in order to determine the improvement in resolution compared to the L2B product. This is done using analysis tools such as statistics, the power spectrum, and derivative fields, and through comparison to other high-resolution data such as synthetic aperture radar (SAR). The improvement of UHR wind retrieval is also explored by reducing ambiguity selection errors and correcting for contamination of wind vectors near land.

Results confirm that ASCAT UHR winds contain high-resolution information that is not present in the L2B product. The resolution improvement is difficult to quantify due to a lack of truth data. Nevertheless, there is evidence to suggest that the resolution is improved by at least a factor of three to 10 km, and perhaps down to 3 or 4 km. It is found through comparison of UHR and SAR winds that (1) both products have common fine-scale features, (2) their comparative statistics are similar to that of L2B and SAR, suggesting that the high resolution content agrees just as well as the low resolution content because the comparison is performed at a finer scale (3) both products have derivative fields that match well, (4) the UHR product benefits from high-resolution direction information, and (5) the UHR product matches better the expected spectral properties of ocean winds.

For the UHR processing improvement methods, the model-based improvement of UHR ambiguity selection allows obvious ambiguity errors to be found and corrected, increases the self-consistency of the wind field, and causes the spectrum to better follow a power law at high wavenumbers. The removal of land-contamination from near-coastal wind vectors allows accurate wind retrieval much closer to land and greater visibility of high-resolution wind features near the coast.

Keywords: remote sensing, scatterometer, radar, ocean winds, high resolution, power spectrum

ACKNOWLEDGMENTS

I wish to thank all those who have provided help and support as I have worked towards completing this thesis. Special thanks to Dr. David Long for his constant guidance during the research and writing process and for always having confidence in my abilities.

I also wish to thank the faculty and staff of BYU, especially the Electrical and Computer Engineering Department. I am grateful for the opportunity to receive an excellent education, and for the many classes I have taken, the professors who have taught them, and the students I have worked with. They have provided me with essential background and understanding in my field of study.

Finally, I want to thank my family for all they have done for me, especially my wife April for her constant support and motivation.

Table of Contents

List of Tables

List of Figures

Chapter 1

Introduction

Wind is an important atmospheric phenomenon related to climate and weather patterns. Wind velocity over the ocean is commonly measured for use in weather reporting and forecasting. Ocean winds are essential for tracking conditions in shipping lanes and for monitoring global wind currents and storm paths.

Near-surface ocean winds interact with many other aspects of the atmosphere and ocean. One important interaction is between wind and waves. Wind over the ocean's surface creates friction, causing the surface to roughen. This generates centimeter-scale waves known as capillary waves. These small waves then lead to larger waves, which continue to propagate. Waves affect navigation and air-sea interaction.

The velocity of ocean winds can be measured in a number of ways. Such measurements are collected by merchant ships and meteorological buoys, which are limited in extent and density of coverage. In more recent years, the development of satellite technology and microwave radar have allowed another form of ocean wind measurement based on satellite radar scatterometry.

Wind scatterometers transmit a microwave radar signal and measure the reflected power, or backscatter, from the ocean surface. This backscatter is directly related to the roughness of the surface from capillary waves caused by ocean winds [1]. The near-surface ocean wind velocity is related to the backscatter measurement by the geophysical model function (GMF), which describes how backscatter varies with both wind speed and direction. After backscatter measurements are taken by the scatterometer, they are combined into a spatial grid, with each grid point called a wind vector cell (WVC) [2]. The GMF is used to determine the wind velocity vector for each WVC. There can be multiple solutions for a given wind vector, called ambiguities, and the correct ambiguity must be chosen using a process called ambiguity selection [3]. The size and spacing of the WVCs determines the spatial resolution of the wind product, which is often in the 25-50 km range.

Wind scatterometers are mounted on satellites. Measurements are made along the radar antenna footprint, and as the satellite travels in its orbit, these measurements form a wide track in the direction the satellite is moving. This measurement track is known as a "swath," and is generally hundreds of kilometers wide.

A benefit of using a transmitted microwave signal is that the ability to receive measurements does not depend on visibility due to the Sun or any other source. Additionally, the microwave frequencies used can largely ignore clouds, rain, and other weather phenomena, although the roughening of the ocean surface by heavy rain may affect measurements.

Spaceborne scatterometers enable the measurement of near-surface ocean winds on a dense, global scale, regardless of visibility and most weather conditions. This in turn facilitates improved weather modeling and forecasting, as winds are an important factor in such models. The high-resolution nature and broad coverage of these scatterometers allow a more continuous and global view of weather and climate trends and behaviors than do others methods such as meteorological buoys and merchant ships. Because of these benefits, many scatterometers have been flown.

The Advanced Scatterometer (ASCAT) is a wind scatterometer that has been in operation since 2007. ASCAT uses a microwave signal frequency in the C-band (5.255 GHz). It is a fan-beam scatterometer, meaning it has multiple antennas fixed at different orientations with respect to the satellite ground track. Similar to most scatterometers, wind vectors are retrieved at standard resolutions of 25 km and 50 km, provided on 12.5 km and 25 km grids. The standard 25 km product, known as Level 2-B (L2B), provides enough information for most applications. However, important high-resolution information about some phenomena can only be captured with a higher resolution product. Such cases include situations with high spatial variation, such as near-coastal regions and storms.

Higher resolution winds may be retrieved from the same scatterometer data that is generally used for these standard resolution winds. This is done using a method known as ultra-high resolution (UHR) processing. UHR processing takes advantage of overlapping measurements from the scatterometer footprint. In the case of ASCAT, the UHR product is provided on a 1.25 km grid. This is ten times finer grid resolution than L2B and ideally provides a data product with frequency information down to a 2.5 km scale, thus supporting these higher resolution applications.

The effective data resolution of these UHR winds needs to be quantified and validated. Validation includes visual inspection and analysis of the power spectrum and statistics of the data set, as compared to both the expected characteristics of ocean winds as well as other high-resolution wind sources. While a spatial sampling rate of 1.25 km allows frequency data down to a 2.5 km resolution, the data quality and noise at these high spatial frequencies must be characterized in order judge what benefit the UHR data is providing.

1.1 Thesis Statement

This thesis attempts to validate the ASCAT UHR wind estimates and determine the improvement in resolution of UHR winds compared to L2B winds. This is done using analysis tools such as statistics, the power spectrum, and derivative fields, and through comparison to other high-resolution data such as synthetic aperture radar (SAR). Additionally, improvements to the UHR wind retrieval process are explored to reduce noise and increase the consistency of the product. Improvement focuses on reducing ambiguity selection errors by matching to a wind field model, and a method is presented to minimize and compensate for the contamination of wind vectors near land.

1.2 Research Summary

Improvement in data resolution due to UHR processing is difficult to quantify. Nevertheless, results suggest that ASCAT UHR winds contain high-resolution information not present in the L2B product. Visual, statistical, and spectral analysis of UHR, L2B, and SAR winds support this claim.

Small-scale visual features can be identified in UHR wind fields that match SAR winds but are not present in L2B winds. This is especially true in near-coastal areas and storms, where more fine-scale wind features are expected. Higher wind speeds in general are also expected in these situations, and this is more evident in UHR and SAR winds than in L2B winds.

Spectral analysis is performed on the various wind fields and compared to the expected spectral properties of ocean winds. Ocean winds are expected to have a spatial spectrum that, on average, follows a power law. This means that the spectrum decreases as a constant power of wavelength. This rate is known as the spectral slope. UHR winds have a spectrum that extends past the L2B spectrum with a constant spectral slope following the power law. For example, the spectral slope of the L2B winds is constant to a wavelength of about $\lambda = 30$ km, the UHR slope continues to at least $\lambda = 10$ km and possibly $\lambda = 4$ km, a significant improvement in either case.

Further statistical analysis and comparison to SAR winds suggests improvement in spatial resolution of the UHR winds compared to L2B winds. Mean wind speeds slightly increase for both UHR and SAR winds due to the preserved high speed, small-scale features that appear in these two products. The correlation to SAR winds is similar for both UHR and L2B winds. This is positive because SAR and UHR are compared on a higher resolution grid than SAR and L2B, suggesting that the added resolution does not degrade the correlation and providing evidence that the higher resolution content of the two products agrees just as well as the low resolution content, even though the high resolution products appear to have more noise.

Promising improvements to UHR wind retrieval are presented with ambiguity selection and land-contamination removal. These are based on previous work for other scatterometer wind products and are applied to this high-resolution ASCAT data set. Land-contamination removal is essential for accurate near-coastal wind retrieval, and the improved ambiguity selection can be further analyzed to determine its usefulness in improving the wind product versus the increased computational requirements.

1.3 Thesis Organization

This thesis is organized as follows. Chapter 2 provides background on the major topics addressed in this thesis, including ocean winds, scatterometry, wind retrieval, the ASCAT scatterometer, UHR processing, and SAR wind retrieval. Chapter 3 examines the ASCAT UHR data set, identifying its unique characteristics and quantifying its enhancement in resolution over the L2B data set. Chapter 4 uses SAR winds to validate the ASCAT UHR winds by comparing the visual characteristics, statistics, and spectra of the two data sets. Chapter 5 explores the improvement of ASCAT UHR wind retrieval by correcting ambiguity selection errors with the aid of a simple wind field model, and Chapter 6 presents a method for removing land contamination in near-coastal ASCAT UHR winds. Finally, Chapter 7 gives conclusions from the work presented in this thesis and offers suggestions for future work.

Chapter 2

Background

This chapter reviews the process and applications of ocean wind retrieval via spaceborne scatterometers. Specifically, it discusses properties of ocean winds and their implications, the basic principles of scatterometry and wind retrieval, and details of the design and implementation of the ASCAT scatterometer in particular. It then describes UHR wind retrieval, including the benefits and limitations of such a high-resolution data set. Lastly, a brief overview is given of SAR imagery and wind retrieval, as compared to scatterometry.

2.1 Ocean Winds

Winds over the ocean are a key factor in many weather and climate applications. These applications include forecasting and tracking weather patterns as well as analyzing and projecting storms and cyclones. Ocean winds have both direct and indirect effects on many other factors in weather and climate models [2]. They affect wave patterns, both immediately and long after the winds have died down. The immediate effect of ocean winds on waves is a simple roughening of the surface caused by friction between the air and the water. These small-scale waves, known as capillary waves, evidence the “grip” of the wind on the ocean surface. This causes larger waves to form and continue propagating without the need for continued wind. Waves are thus related to wind, ocean currents, atmospheric pressures, temperature, and other geophysical and meteorological phenomena.

2.1.1 Power Spectrum

Any signal may be represented by its power spectrum, which describes its temporal or spatial properties in terms of the power present at different frequencies or wavenumbers. For a typical one-dimensional signal, the spectrum may be generated as simply the squared

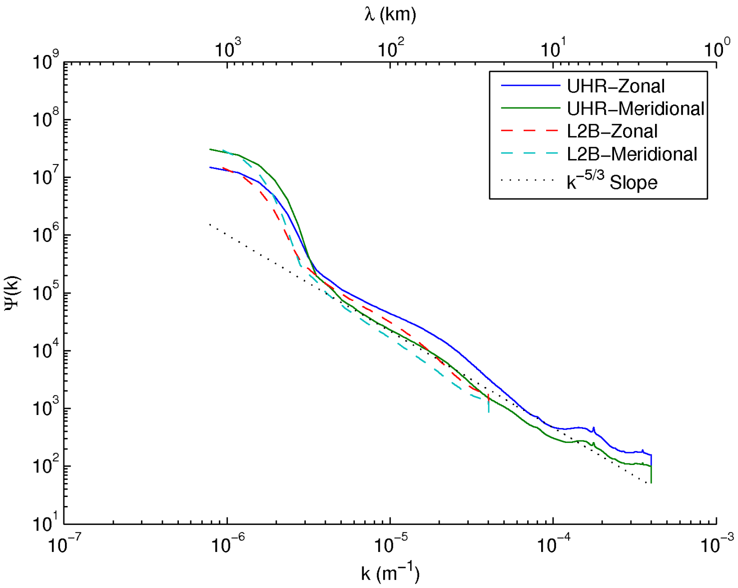

Figure 2.1: The average spatial power spectrum of high and low resolution ocean winds measured using the ASCAT scatterometer.

magnitude of the Fourier transform. Ocean winds, however, are represented spatially as a two-dimensional vector field rather than a one-dimensional scalar. In general, this type of signal has a two-dimensional spectrum that varies with vector direction. Nevertheless, a one-dimensional spectrum is easier to analyze and is the most common form in which ocean wind spectra are presented. A one-dimensional scalar signal is achieved by separating the vector field into two scalar components and then treating the individual rows of the two-dimensional signal as a one-dimensional signal. The scalar components of the wind field are the zonal component (wind blowing in the west-east direction, usually denoted as u) and the meridional component (north-south, usually denoted as v). Each of these components is generally analyzed in the along-track direction of the measuring instrument.

Ocean winds are expected to have a one-dimensional spatial power spectrum with an approximate slope of $k^{-5/3}$, where k is the wavenumber of the signal [4–6]. This is true of both the zonal and meridional components (see Figure 2.1). This type of decaying spectrum is known as a red spectrum and is said to follow a power law. It implies that wind fields over the ocean are dominated on average by low-order characteristics and variations; in general, the high-resolution power is relatively insignificant. This is due to an energy cascade that transfers energy from one scale to other scales through turbulence. A small increase can sometimes be seen in the mesoscale range ($<$ 50 km) [6]. At very small scales turbulence dominates, causing the spectrum to increase again, after which the energy cascade eventually dissipates into heat at the molecular scale. This happens at scales much smaller than are typically measured ($<$ 20 m).

It is important to remember that the behavior described is only true on average, and any given wind field may in fact contain more or less energy at high spatial frequencies than the power law would indicate. This is especially true of extreme wind events such as storms and tropical cyclones [7], or in near near coastal areas where land features may cause jets or otherwise affect wind currents [8, 9].

2.1.2 Vorticity and Divergence

Vorticity and divergence are important derived variables from ocean winds and describe spatial trends in the local wind velocity. According to the Helmholtz theorem, these values decompose the velocity field into rotational and irrotational components. Vorticity is defined as the curl of the wind velocity field and describes the rotational energy of the winds at any given point. This rotation measurement helps to quantify the true behavior of the winds and, when combined with temperature measurements in what is known as potential vorticity, is a key factor in forecasting the creation and growth of storms and tropical cyclones. Figure 2.2 shows the wind vectors, vorticity, and divergence for a particular wind field in the Gulf of Alaska. High magnitude vorticity values correspond to areas with sharp transitions or high variation in either speed or direction.

Vorticity is a derivative field measuring the rotational component of a velocity field about a given point. The vorticity ($\boldsymbol{\zeta}$) is given by

$$\boldsymbol{\zeta} = \nabla \times \mathbf{w},$$

where $\nabla\times$ is the curl operator and $\mathbf{w}$ is the wind velocity. Although this field is a three-dimensional vector field in general, ocean wind vector fields are generally given in only two dimensions (x and y), causing the vorticity vectors to only have a component in the z

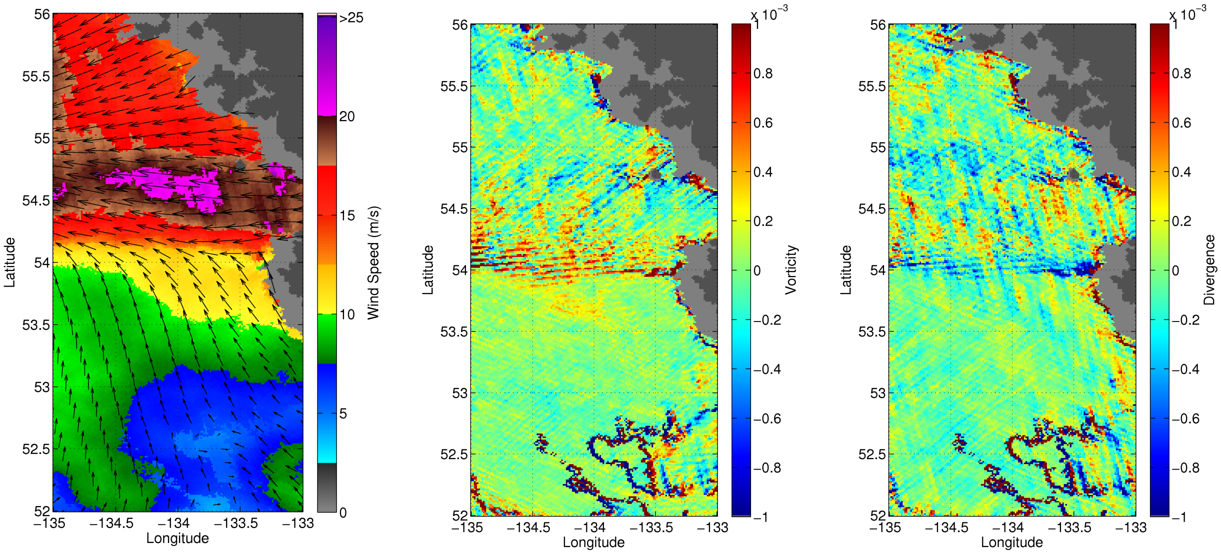

Figure 2.2: A wind field (left) along with its corresponding derived vorticity (middle) and divergence (right) fields. This example is shown because of large changes in speed and direction, which better illustrate the derivative behavior.

direction and allowing it to be expressed as a scalar (ζ), given by

$$\zeta = \frac{\partial v}{\partial x} - \frac{\partial u}{\partial y},$$

where u and v are, as before, the x and y, or zonal and meridional, components of $\mathbf{w}$.

Divergence, denoted as δ, is another derivative field that measures how much a velocity field is diverging from or converging toward a given point. It is the irrotational part of the Helmholtz decomposition. Like vorticity, the divergence of ocean winds helps to describe the true behavior of the winds and is related to weather trends and storm formations. Divergence is a scalar value given by

$$\delta = \nabla \cdot \mathbf{w},$$

where $\nabla\cdot$ is the divergence operator. Again, as wind vectors are generally given in two dimensions, this can be simplified to

$$\delta = \frac{\partial u}{\partial x} + \frac{\partial v}{\partial y}.$$

Positive divergence values correspond to diverging winds, while negative divergence values correspond to converging wind.

There are some important considerations when computing the vorticity and divergence of a wind vector field. A wind vector field is in general sampled on a discrete spatial grid. Because of this, the equations must be converted to their discrete form, and spatial differences must be calculated rather than derivatives. The formulas can then be given as first order difference equations by

$$\hat{\zeta}_{i,j} = \left(\frac{v_{i+1,j} - v_{i-1,j}}{x_{i+1,j} - x_{i-1,j}}\right) - \left(\frac{u_{i,j+1} - u_{i,j-1}}{y_{i,j+1} - y_{i,j-1}}\right)$$

and

$$\hat{\delta}_{i,j} = \left(\frac{u_{i+1,j} - u_{i-1,j}}{x_{i+1,j} - x_{i-1,j}}\right) + \left(\frac{v_{i,j+1} - v_{i,j-1}}{y_{i,j+1} - y_{i,j-1}}\right),$$

where $\hat{\zeta}$ and $\hat{\delta}$ are discrete approximations of the vorticity and divergence, and i and j are the horizontal and vertical coordinates of the grid location at which the value is being calculated.

It is also important to consider the coordinate grid in which the wind field is defined. In order for the calculated values to be correct, the orientation of coordinate grid onto which the wind vectors are sampled (i, j) must match the coordinate grid in which the wind vector components and distances are defined (x, y, u, v). In general this is not the case, as the sample grid is often oriented in the direction of travel of the measuring instrument, while u and v are in east and north directions and x and y may be in either longitude and latitude or physical distance. This may be compensated for by rotating one of the coordinate grids to match the other. This should not affect the values as vorticity and divergence are rotationally invariant [10].

Lastly, on large scales ocean wind divergence is on average considered to be zero. This is due to conservation of mass and the fact that wind fields are two-dimensional. In practice, however, this may not be the case because of noise, vertical wind movement, or other causes. It is still, however, generally very close to zero on average.

2.1.3 Measuring Ocean Winds

Proper analysis of ocean winds, as well as the ability to use them in weather models, requires a method of measurement that is accurate and provides enough coverage to extract useful characteristics and trends. There are many ways to measure winds, both historic and modern, and with varying degrees of coverage and accuracy. Highly sparse and localized forms of measurement come from ships and and meteorological buoys. Dense global coverage can only be achieved with spaceborne remote sensing instruments, the most common of which are scatterometers.

Historically, most ocean wind measurements were performed by merchant ships. These measurements, while helpful for observing weather conditions and determining travel routes, are often inaccurate and are localized to wherever the ships happen to be at the time [11]. Their inaccuracy comes from many factors, including human error, mast height, faulty equipment, and ship movement. Also, the localized nature of these measurements causes bias in the data, as ships generally stick to certain routes and avoid extreme weather [2].

Moored meteorological buoys are also very localized. There are relatively few of them, and they tend to be concentrated in coastal regions in the northern hemisphere [2]. They do, however, provide accurate wind measurements and are often included in weather prediction models. They are also used to validate the low-order trends of other forms of wind measurement.

As mentioned, only satellite instruments can retrieve global, high-resolution wind data. Several types of these remote sensing devices can be used to estimate wind speed, including altimeters, radiometers, scatterometers, and synthetic aperture radar (SAR). Because of their ability to resolve both wind speed and direction, scatterometers are generally the preferred instruments for wind measurement. Scatterometers are known to be fairly accurate, and their accuracy is mostly independent of conditions and location [11]. The following section discusses the basic principles of scatterometry.

2.2 Scatterometry

Scatterometers are active remote sensing instruments, meaning that they are radar devices designed to transmit microwave pulses toward a surface and measure the reflected power, or backscatter, in order to determine the geophysical properties of the surface in question [1]. Rather than use the returned power directly, however, the backscatter coefficient, or normalized radar cross section (σ^0), is estimated. This value is more directly related to the geophysical properties of the surface and can be thought of as the return power normalized by the transmitted power and the area of the target. The backscatter coefficient can be calculated using the radar equation, given by

$$\sigma^0 = \frac{(4\pi)^3 R^4 L P_r}{P_t G^2 \lambda^2 A}, \tag{2.1}$$

where R is the range to the target surface, L is system loss, P_r is the received power, P_t is the transmitted power, G is the antenna gain, λ is the wavelength of the transmitted signal, and A is the illuminated area of the target surface [1].

The σ^0 value returned for a single microwave pulse represents the radar cross section for the illuminated area, or the 3 dB beamwidth of the antenna. This relatively large measurement area can be subdivided by time-filtering the return pulse. This is known as range resolution since parts of the target area at farther distances have a longer time delay, allowing target discrimination based on range.

Resolution is also obtained in the angular direction and depends on the beamwidth and the time between pulses. Additionally, Doppler processing can be used to further enhance the resolution within a single pulse, but in the direction of travel [1]. A single σ^0 measurement, after range, angular, and Doppler resolution, is a weighted integral of the surface σ^0 surrounding the measurement location. This weighting is determined by the antenna beam response and resolution processing and is known as the spatial response function (SRF).

2.2.1 Wind Retrieval

As mentioned, the value of σ^0 depends on the properties of the surface being illuminated. These properties may include vegetation, moisture, ground type, roughness, and more. In the case of measurement over the ocean, σ^0 increases with surface roughness, which

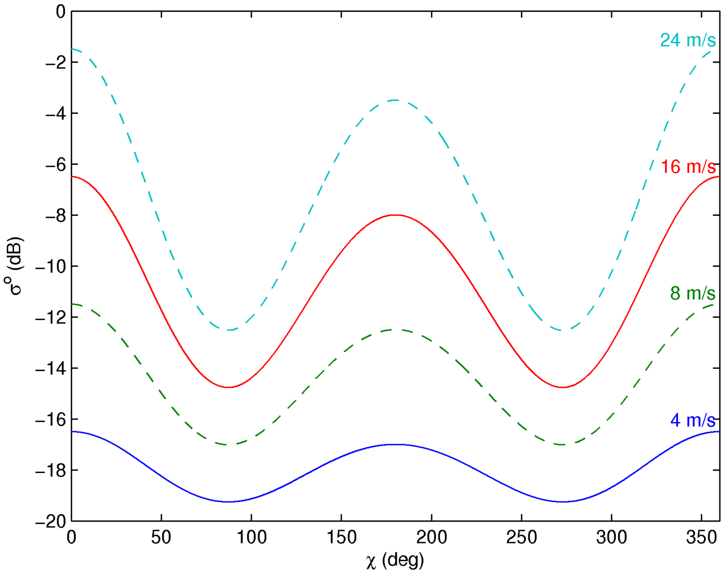

Figure 2.3: An example GMF, showing the variation of backscatter coefficient (σ^0) with relative wind direction (χ) and speed ($|U|$).

consists of the small-scale capillary waves caused by ocean winds. The relationship between the velocity of these ocean winds and σ^0 is known as the geophysical model function (GMF).

The GMF must be known in order to derive wind speed and direction after retrieving σ^0. It is a very complicated function that depends on many variables and is not entirely understood. In theory, it should be able to be derived analytically, and much work has been done in this area. However, due to limited knowledge, the models that are used for this function are derived from observed data [2]. Based on current understanding of these empirical relationships, the GMF can be generally represented as

$$\sigma^0 = f(|U|, \chi, ...; \theta, f, pol), \tag{2.2}$$

where $|U|$ is wind speed, χ is the azimuth angle between the incident wave and the wind vector, ... represents the effects of non-wind variables, θ is the incidence angle, and f and *pol* are the frequency and polarization of the incident wave.

Because of the shape of the GMF, there are a range of possible wind speeds and directions for a given σ^0 measurement. Figure 2.3 shows an example of the relationship between σ^0 and χ for several different wind speeds. Any particular relationship holds only

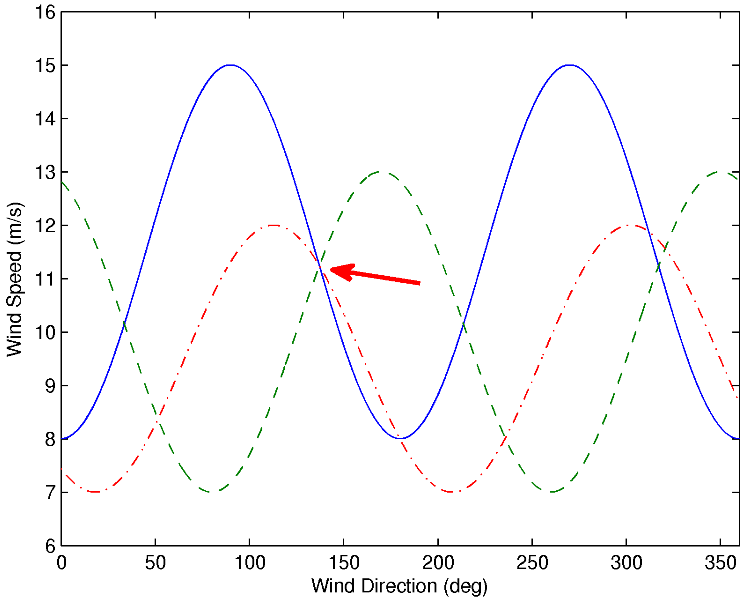

Figure 2.4: An example of the intersection of multiple σ^0 measurements.

for a specific incidence angle, frequency, and polarization. If these variables are changed, the plot has similar periodic behavior, though shifted and scaled. This is only valid, however, for θ between about 20° and 65°, and for a signal wavelength comparable to that of the capillary waves on the ocean surface (typically frequencies in the $\mathrm{K_u}$-band or C-band).

In order to resolve wind speed and direction from the range of possibilities, multiple σ^0 measurements are used, taken from antennas at different azimuth angles. Sometimes different incidence angles and polarizations are used as well. In this way, intersecting points can be found from the various solutions, ideally resulting in a unique solution (see Figure 2.4). Unfortunately, for a noisy signal there are generally still multiple solutions of nearly the same speed but different directions. These are known as ambiguous vectors and must be resolved using additional processing. This processing includes such strategies as median filtering, matching to known winds, and matching to predetermined wind field models [3, 12].

The GMF is only valid for open water conditions, and consideration must be made for near-coastal measurements. These measurements may be centered over the ocean, but have an SRF that extends over land, contaminating the ocean σ^0 value. Even a small amount of overlap can greatly affect the backscatter because land σ^0 values are generally much higher than ocean σ^0 values [13]. This effect is known as land contamination, and must be addressed

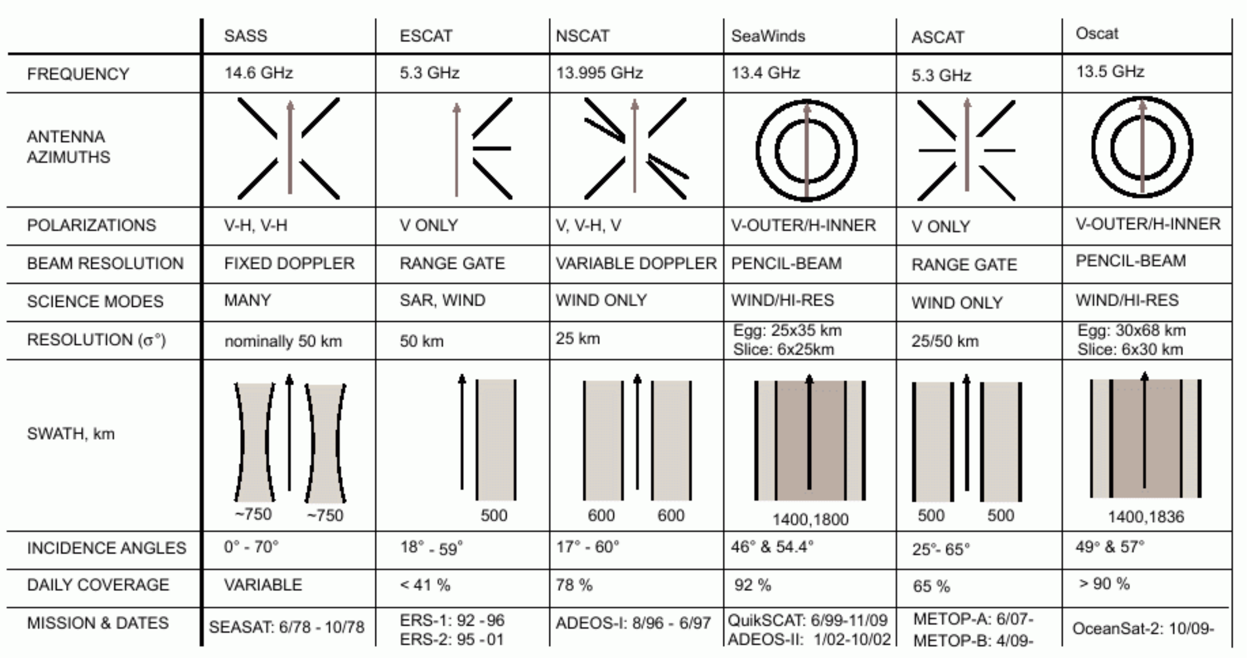

	SASS	ESCAT	NSCAT	SeaWinds	ASCAT	Oscat
FREQUENCY	14.6 GHz	5.3 GHz	13.995 GHz	13.4 GHz	5.3 GHz	13.5 GHz
ANTENNA AZIMUTHS						
POLARIZATIONS	V-H, V-H	V ONLY	V, V-H, V	V-OUTER/H-INNER	V ONLY	V-OUTER/H-INNER
BEAM RESOLUTION	FIXED DOPPLER	RANGE GATE	VARIABLE DOPPLER	PENCIL-BEAM	RANGE GATE	PENCIL-BEAM
SCIENCE MODES	MANY	SAR, WIND	WIND ONLY	WIND/HI-RES	WIND ONLY	WIND/HI-RES
RESOLUTION ($\sigma°$)	nominally 50 km	50 km	25 km	Egg: 25x35 km Slice: 6x25km	25/50 km	Egg: 30x68 km Slice: 6x30 km
SWATH, km	~750 ~750	500	600 600	1400,1800	500 500	1400,1836
INCIDENCE ANGLES	0° - 70°	18° - 59°	17° - 60°	46° & 54.4°	25°- 65°	49° & 57°
DAILY COVERAGE	VARIABLE	< 41 %	78 %	92 %	65 %	> 90 %
MISSION & DATES	SEASAT: 6/78 - 10/78	ERS-1: 92 -96 ERS-2: 95 -01	ADEOS-I: 8/96 - 6/97	QuikSCAT: 6/99-11/09 ADEOS-II: 1/02-10/02	METOP-A: 6/07- METOP-B: 4/09-	OceanSat-2: 10/09-

Figure 2.5: Several scatterometer missions and their characteristics. From [1].

to allow accurate wind retrieval near land. Land contamination is considered in more detail in Chapter 6.

In order to complete the process of wind retrieval into a grid of wind vector cells, the specific geometry and characteristics of the scatterometer in use must be known. The following section introduces several major satellite scatterometers that have been used to retrieve wind data.

2.2.2 Scatterometer Missions

Many spaceborne scatterometers have been used for wind retrieval in the last few decades. Figure 2.5 summarizes several major scatterometer missions and their characteristics. The first wind scatterometer, called the Seasat-A satellite scatterometer (SASS), was launched by the National Aeronautics and Space Administration (NASA) on the Seasat mission in June 1978. This mission unfortunately failed after four months, but it has been succeeded by many more missions launched by both NASA and the European Space Agency (ESA).

Even though SASS was in use for such a short amount of time, useful lessons were learned from the data gathered and were applied in the implementation of later scatterometers. For example, SASS had antennas at two orthogonal azimuth angles in each side-looking illumination area (known as swaths). It was found that two measurements at orthogonal azimuth angles are not able to unambiguously resolve wind direction (looking again at Figure 2.4, any two curves have several intersections).

Scatterometers after SASS have used more than two measurement angles. There are two general antenna schemes used to achieve multiple azimuth angles. They have their antennas arranged as either a fan-beam or a pencil-beam. A fan-beam radar instrument has multiple fixed antennas oriented in different directions corresponding to the azimuth angles from which measurements are taken. Each antenna may take measurements at a range of incidence angles using range resolution, as discussed at the beginning of Section 2.2. As the satellite travels in its along-track direction, there are overlapping measurements from each azimuth direction and these are used to retrieve wind for a specific grid location. SASS was a fan-beam instrument with two antennas. Subsequent fan-beam scatterometers have generally used three. A pencil-beam radar instrument has antennas that physically rotate, allowing measurements at a wide range of azimuth angles, though with a fixed incidence angle. They often have two rotating beams, an outer and inner beam, at different incidence angles and different polarizations. This layout provides a variety of measurement types from which to retrieve winds, as there are overlapping measurements from the forward and rear sections of both rotating paths.

Different scatterometers also use microwave signals from different frequency bands. Scatterometers launched by NASA are typically $\mathrm{K_u}$-band at around 13-14 GHz, and those launched by ESA are typically C-band at around 5 GHz. Higher frequency signals are more sensitive to smaller ocean surface waves. This means that $\mathrm{K_u}$-band scatterometers are more sensitive to low wind speeds. However, they are also more sensitive to atmospheric effects and rain contamination, as rain contributes to surface roughness at a very small scale [11].

This thesis focuses on ASCAT, a European fan-beam scatterometer operating in the C-band. The following section discusses ASCAT in more detail.

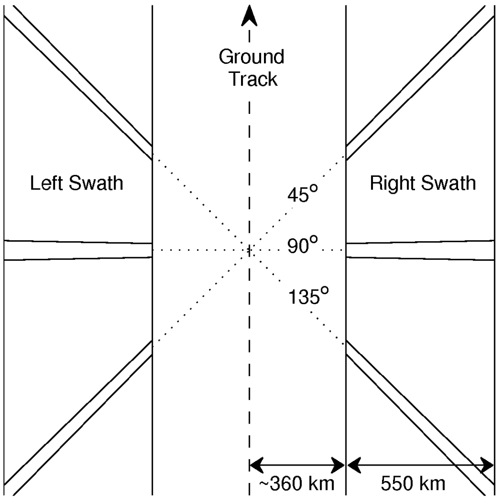

Figure 2.6: ASCAT swath geometry. Adapted from [14]

2.3 ASCAT Scatterometer

The Advanced Scatterometer (ASCAT) is a C-band wind scatterometer that operates at 5.255 GHz with vertical polarization. It uses a fan-beam antenna scheme with backscatter measurements at three azimuth angles of 45°, 90°, and 135°. As discussed in the previous section, using three azimuth angles allows for easier resolution of wind direction. Measurements are taken in each of two 550 km-wide swaths on either side of the satellite ground track. These wide swaths, separated from the ground track by about 360 km, provide measurements at an incidence angle range of 25° to 65° [14]. Figure 2.6 shows the swath geometry of ASCAT. Previous European scatterometer missions took measurements on only one side of the satellite, and using two swaths more than doubles the coverage of previous missions. ASCAT covers 65% of the Earth daily and achieves near global coverage in five days [15].

Within the measurement swaths, each beam is divided into 256 measurement locations, or nodes, using range resolution processing, as explained in Section 2.2. Only 192 of these, however, fall into the 550 km swath and are used. Measurements outside the swath have incidence angles outside the acceptable range. Figure 2.7 illustrates these measurement nodes and the extent of the measurement area (SRF) for each one. The size of and distance between measurements varies with both incidence angle and azimuth angle, and they generally overlap. The pulse repetition frequency (PRF) and along-track averaging for

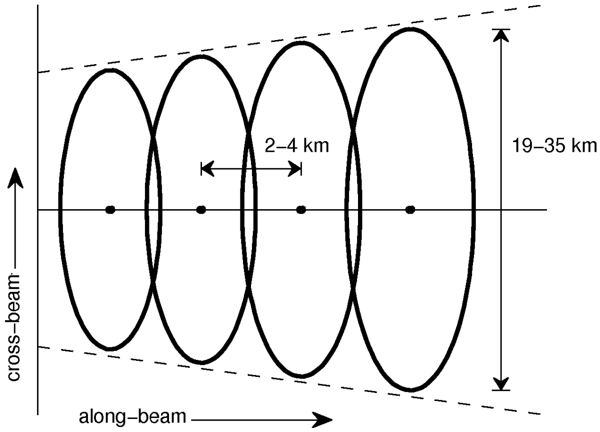

Figure 2.7: ASCAT beam measurement geometry. Adapted from [17].

ASCAT correspond to measurements taken every 5.6 km in the along-track direction. The radar product containing these full-resolution, geo-located backscatter measurements along each beam is known as the "Level 1-B Full Resolution Product," and is denoted as L1B SZF, or just SZF. Before wind vector fields are estimated from the measured σ^0 data, the measurements for each beam are spatially averaged into a swath-oriented grid, where all measurement nodes whose centers lie in a grid location are averaged together. This is done at two different grid resolutions which are known as SZO for the "operational resolution" product (25 km grid) and SZR for the "research resolution" product (12.5 km grid) [16].

ASCAT is part of the European Meteorological Operational (MetOp) mission, which is a joint program between ESA and the European Organisation for the Exploitation of Meteorological Satellites (EUMETSAT). There are three planned MetOp satellites, which are part of the EUMETSAT Polar System (EPS). MetOp-A was launched in October 2006 and MetOp-B in September 2012. Both have identical ASCAT instruments on board. MetOp-C is due to be launched in 2017. These are all sun-synchronous, polar orbiting satellites with many meteorological instruments in addition to ASCAT. [18].

ASCAT has been in operation since 2007. Wind data is processed in conjunction with the National Oceanic and Atmospheric Administration (NOAA), and wind estimates are provided at spatial resolutions of 50 and 25 km, given on 25 km and 12.5 km grids, respectively. The standard resolution wind product on a 12.5 km grid is known as Level 2-B (L2B).

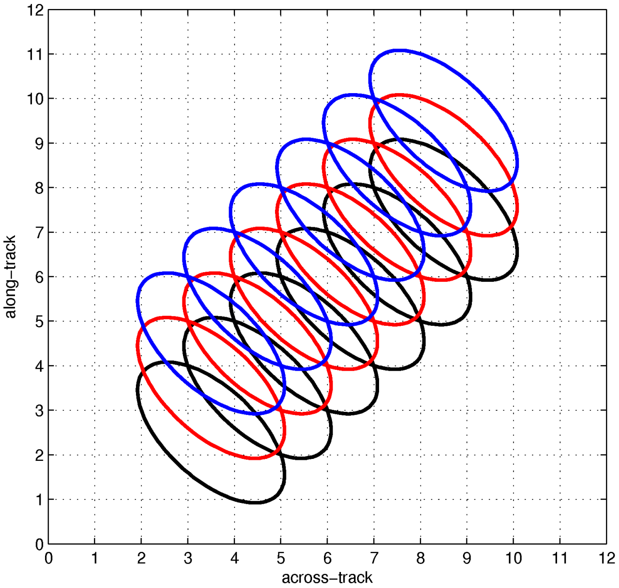

Figure 2.8: UHR processing takes advantage of overlapping measurements in ASCAT and averages all measurements touching a given grid location. L2B only averages those whose centers touch a grid location.

2.4 UHR

The standard L2B product provides enough information for many applications. However, in some cases it may be useful to have a wind product with a better spatial resolution, especially in situations with high spatial variation in ocean winds, such as near-coastal regions and storms. This is not feasible using the standard L2B method, in which the measurement nodes are averaged in a grid based on their center location. Instead, ultra-high resolution (UHR) processing is used.

UHR processing is based on a method developed by Long, Hardin, and Whiting for generating increased resolution σ^0 imagery using scatterometry [19]. This process enhances the spatial resolution of the σ^0 measurements and allows a finer σ^0 grid, after which high-resolution wind vectors are retrieved using maximum likelihood retrieval [1]. In UHR processing, all measurements that overlap the center of a WVC are combined using a weighted average based on the SRF of each measurement. This is done separately for each of the three ASCAT beams in each swath. This exploits the overlap between ASCAT measurements in the along-beam and along-track directions, as illustrated in Figure 2.8 [19–22]. ASCAT UHR data is reported on a 1.25 km grid, ten times the grid resolution of the L2B product.

Wind retrieval is performed using the same wind vector estimation method as L2B [22]. For a given WVC, a maximum likelihood estimation technique is used to find a wind vector solution from the three σ^0 values and the GMF [1]. This thesis explores the data resolution of UHR wind estimates, including the effects of noise and the validity of the high-resolution variations that are not present in L2B.

2.5 SAR Wind Retrieval

Another way to retrieve very high resolution ocean wind data is to use synthetic aperture radar (SAR). SAR wind retrieval is not as common as scatterometer wind retrieval because with SAR it is much more difficult to estimate wind direction. Nevertheless, SAR allows imaging at a finer resolution than scatterometry, and has been used for studies of near-coastal and other fine-scale winds [8, 9, 23, 24].

SAR instruments, like scatterometers, are remote sensors that transmit microwave pulses toward a surface and measure the reflected power, or backscatter, at the point of transmission. For the surface or target in question, the normalized radar cross section (σ^0) is determined using the radar equation (see Section 2.2). The key difference between a SAR and a real aperture radar, such as a scatterometer, is that SAR makes use of the movement of the aircraft or satellite on which it is mounted and coherently combines multiple pulses in order to “synthesize” a long array antenna. This allows much finer resolution in the along-track direction [1].

The along-track spatial resolution of a radar image depends on the beamwidth of the antenna used. For a real aperture antenna, the beamwidth is decreased (and the resolution improved) by increasing the length of the antenna. An equation for the resolution of real aperture radar can be given as

$$r_{rar} = \frac{\lambda R_0}{l}, \tag{2.3}$$

where λ is the signal wavelength, R_0 is the minimum range to the target, and l is the antenna length. This antenna length can quickly become unrealistic when a very fine resolution is desired. SAR has a narrow beamwidth because it treats multiple pulses as an array antenna. This beamwidth is further decreased by increasing the number of pulses that illuminate the same target location, or the dwell time of a single pulse on a given location. This is accomplished by increasing the beamwidth of the antenna, meaning that a smaller antenna will actually cause finer resolution when using SAR. Optimal SAR resolution is given by

$$r_{sar} = \frac{l}{2}, \tag{2.4}$$

showing a that it is proportional to the true antenna length [1,25].

As with scatterometers, wind vector estimates can be retrieved using the GMF and the retrieved SAR σ^0. However, while scatterometers measure backscatter at multiple azimuth angles in order to infer wind direction, SAR backscatter is observed at only one azimuth angle. This does not allow a unique wind vector solution (see Section 2.2.1). In order to achieve a unique solution, a previously known wind direction becomes an input and wind speed is estimated from the SAR backscatter using the GMF. These input wind directions are typically obtained in one of two ways. The first is from an outside source such as numerical weather models, and the second uses linear features in the SAR image itself. There are tradeoffs between these two methods. The linear features in the SAR images are not always present and may be affected by other atmospheric and oceanographic conditions, and model wind directions are usually at a much lower resolution than SAR data [1,8,23,24].

2.6 Summary

This chapter provides basic background on the tools and principles of ocean winds and scatterometry that are used in this thesis. Ocean winds, as an important metric for weather and climate applications, have unique properties that are used in the following chapters to examine the quality of UHR data retrieved from the ASCAT scatterometer. These properties can be studied using analysis tools such as the power spectrum and vorticity.

The dense, global coverage of ASCAT is ideal for analyzing both small and large scale wind properties and possible improvements in overall quality of wind estimates. Additionally, UHR data, with a pixel size that is one tenth that of the standard resolution product, has the potential to expand the usefulness and application of ASCAT winds. However, the true data resolution has not previously been quantified, nor has the increase in resolution been validated. The tools and principles discussed previously can help to accomplish this and find ways to improve the retrieval of these high-resolution winds. Further background, if needed for individual analysis techniques, is provided in the appropriate chapter.

Chapter 3

UHR Resolution Enhancement for ASCAT Winds

The significant reduction in pixel size for UHR winds compared to L2B winds for ASCAT ideally allows visibility of higher resolution features. However, UHR processing is also expected to add noise, and due to the non-linear wind retrieval there is an uncertain increase in the effective resolution of the resulting data. This chapter investigates the resolution increase in UHR by comparing it to the original L2B data and analyzing the visual features and spectrum. In this way we attempt to quantify the true increase in data resolution. Though the UHR process has been investigated for other scatterometers [20–22, 26–28], very little previous analysis has been done for the ASCAT UHR wind product. Some investigation has been performed on the low resolution product [29] and using instrument models [30], but this is the first attempt at validation of the ASCAT UHR data product. Chapter 4 extends this investigation by comparing the UHR data to independent high-resolution wind data gathered from SAR.

3.1 L2B and UHR Data Sets

The process of wind retrieval for ASCAT is described in detail in Chapter 2. For convenience, relevant information is presented again here. The standard L2B wind product is retrieved by averaging together all σ^0 measurements with centers located in a given 12.5×12.5 km grid location. This is done separately for each of the three antenna azimuth angles in a swath, and the GMF is used to find a unique wind vector solution from the three σ^0 values. If a unique solution cannot be found due to noise or other factors, multiple solutions with equal likelihood are found and other methods known as ambiguity selection are used to select a single estimate.

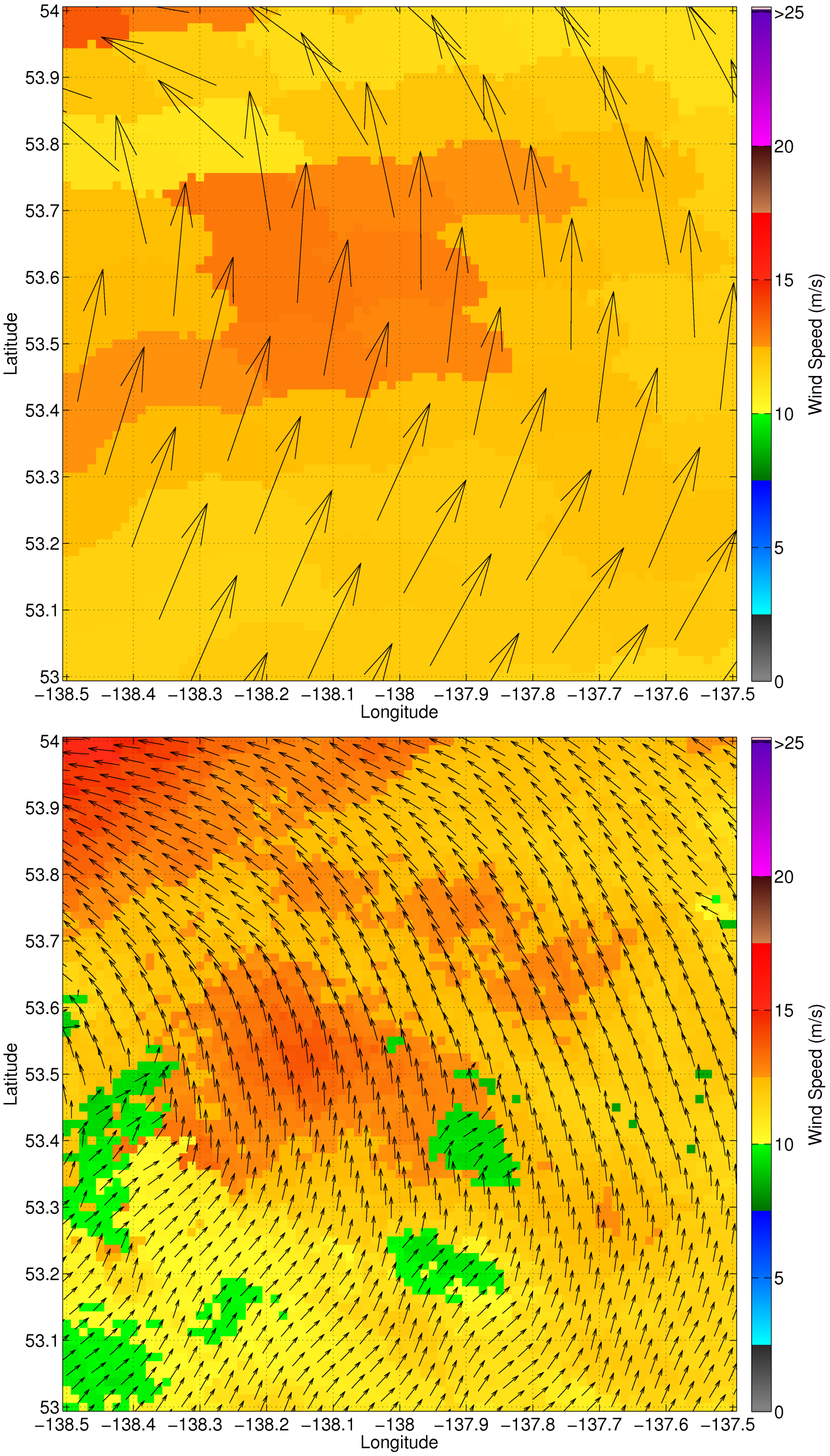

Figure 3.1: L2B (top) and UHR (bottom) winds retrieved from ASCAT on 5 Feb 2013 near the coast of Alaska and British Columbia. The image highlights the difference in spatial resolution. L2B vectors are shown at L2B spacing, while UHR vectors are downsampled to twice the spacing of UHR to increase visibility. The vectors are located at the base of the arrows, and are scaled according to grid spacing. The background color represents wind speed.

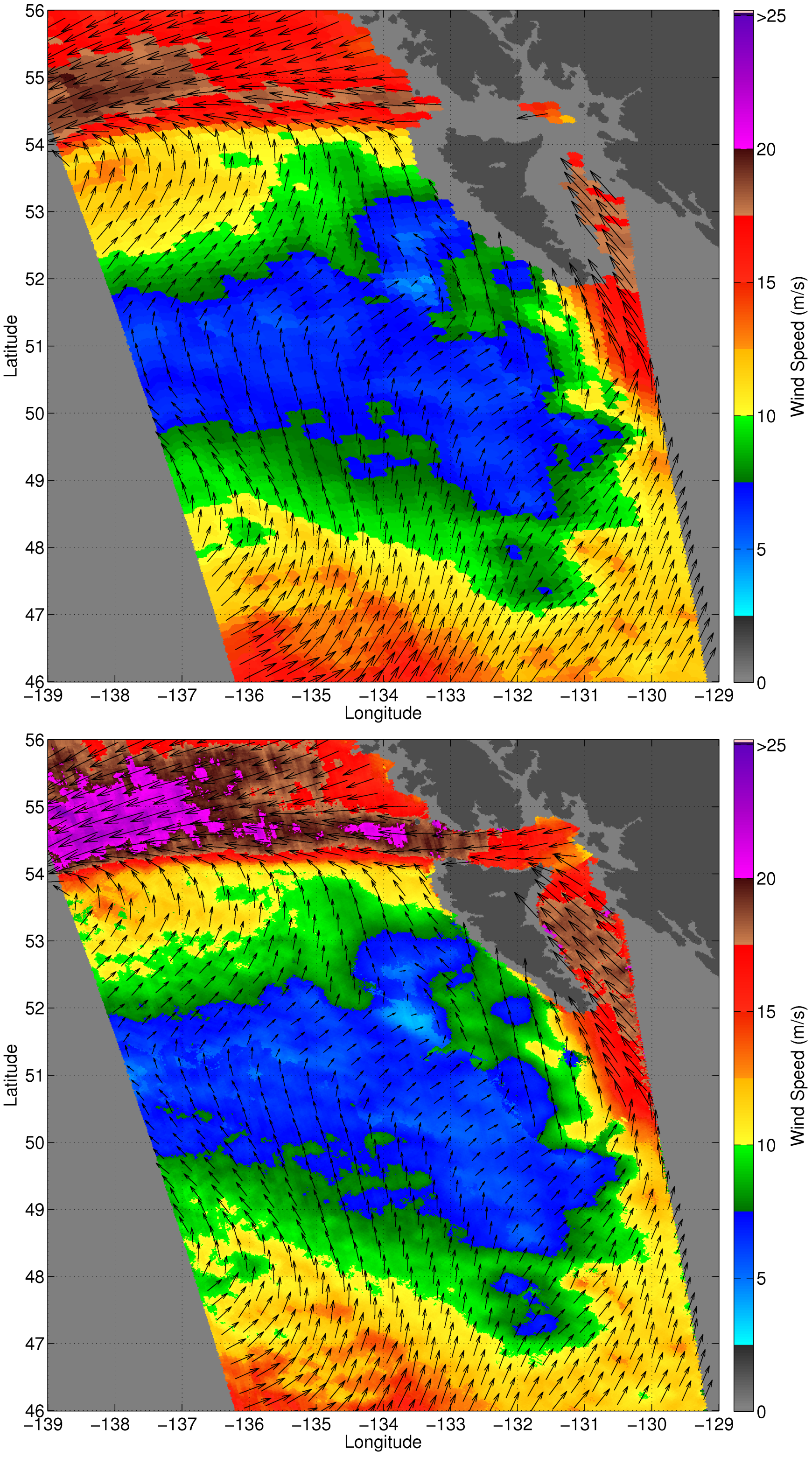

Figure 3.2: L2B (top) and UHR (bottom) winds from ASCAT. This is from the same time and location as Figure 3.1, but showing a wider view area. Direction arrows are downsampled to 0.25° spacing to increase visibility.

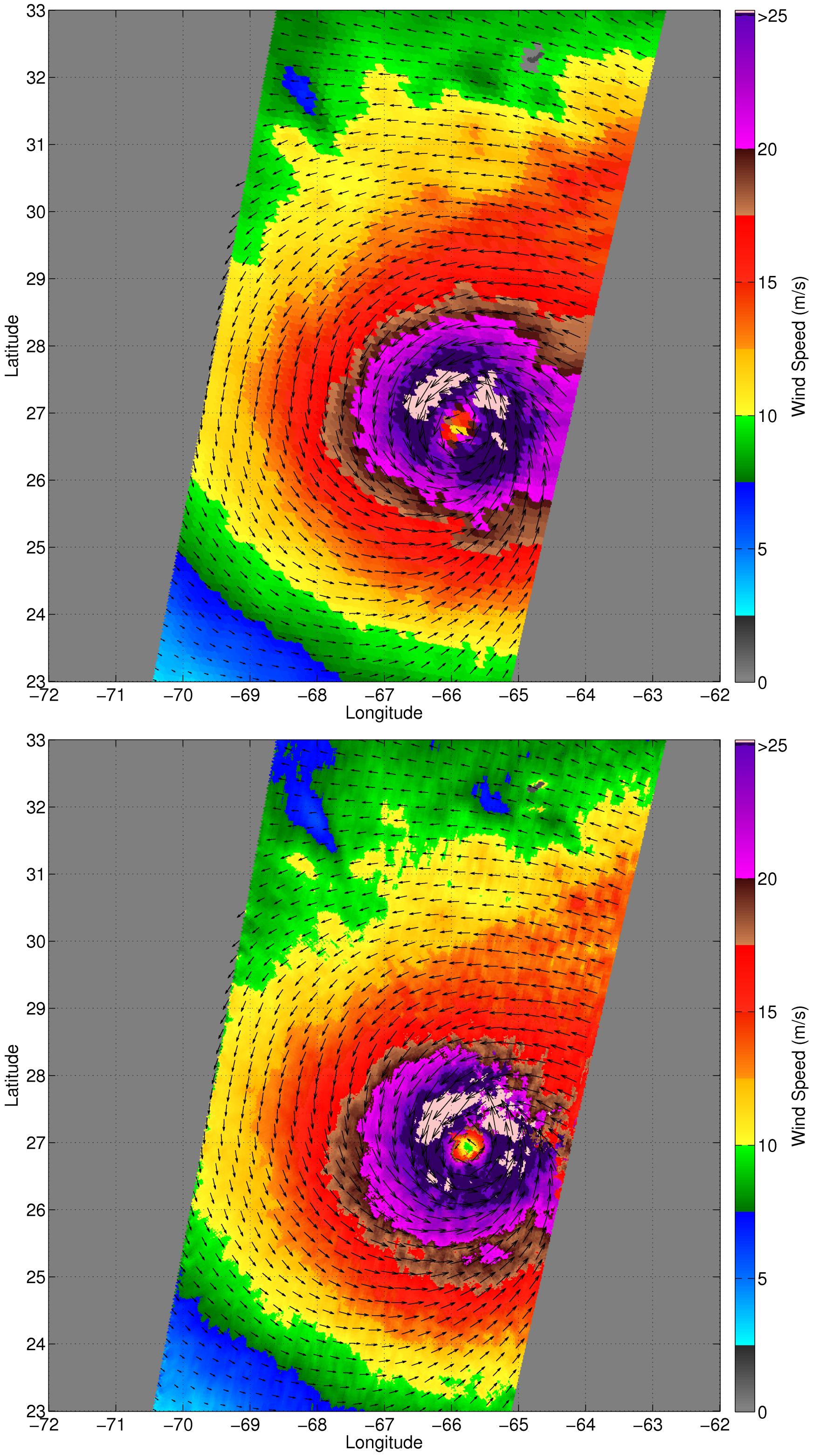

Figure 3.3: L2B winds (top) and UHR winds (bottom) retrieved from ASCAT on 6 Sep 2011 in the North Atlantic. The storm shown is Hurricane Katia. UHR data shows more detail for a high-resolution wind event such as a storm. Direction arrows are downsampled to 0.25° spacing to increase visibility.

In the case of UHR, the σ^0 value at a grid location is determined by the response-weighted average of all measurements with any part overlapping the center of the cell, with weights and extent based on the SRF of the measurement. This is true even if the center of the measurement lies in a different cell. A much smaller 1.25×1.25 km grid is used for σ^0 averaging, taking advantage of the large amount of overlap between measurements [19]. Wind vectors are found by the same method as with L2B, using the GMF.

Figures 3.1 to 3.3 highlight the difference in spatial resolution between UHR and L2B wind estimates for a typical wind field. While some analysis has been done for UHR winds from other instruments [26], a detailed visual analysis has not been done previously for ASCAT UHR winds. Such a visual comparison is not a rigorous validation of the data, but provides a preliminary demonstration of increased resolution and a basis from which to pursue further analysis.

Figure 3.1 shows 1° longitude by 1° latitude images of both L2B and UHR wind fields. The high resolution features are more clearly defined in the UHR image. Color boundaries and contour lines show more detail, and higher resolution variations are seen in both wind speed and direction.

Figure 3.2 shows similar properties, but from a wider view area. Additionally, local maxima and minima in wind speed are sometimes more extreme. Specifically, in the bottom left of the image, the UHR winds have more variation than the L2B winds. Also, in the top left of the image, the UHR speeds are significantly higher, which may be a true property of the wind that can be seen due to spatial averaging on a finer scale. These same types of differences are seen throughout the images in Figure 3.2, while the large scale trends and features are the same.

UHR processing also allows wind estimates to be retrieved closer to land. In general, σ^0 values over land are much higher than those over ocean water. Any ASCAT measurement over water with an SRF that is too close to land is greatly affected by the contamination of its ocean σ^0 value by leakage from the land σ^0 value. Such a measurement is said to have land contamination. Land-contaminated measurements must be excluded by both L2B and UHR wind retrieval processes [13]. However, as explained previously, UHR processing uses the SRF and performs a weighted average of all measurements overlapping a grid location, while L2B only uses the center location of each measurement. Therefore, UHR winds may be retrieved closer to land according to the distance that the measurement SRF extends from its center.

Figure 3.3 shows an image of winds in a tropical storm in the North Atlantic. Storms tend to have more high-resolution wind features than many other weather patterns due to their high wind speeds and cyclonic nature, and therefore provide a good example for comparing the resolution of two wind products [27, 28]. As in Figure 3.2, UHR wind speed contours are more detailed with higher frequency variations. Additionally, the eye of the storm is more clearly defined in the UHR image (see [28]), and the pattern of decrease in wind speed away from the center is more detailed. The highest wind speeds in a storm such as this have low accuracy when measured by scatterometers, as the accuracy of the GMF begins to degrade at such high speeds. Nevertheless, the shape of the storm appears in greater detail in the UHR image, and the highest speeds make up a small percentage of the image. Rain may also affect accuracy, although ASCAT is less affected by rain than some other scatterometers because it operates in the C-band.

The basic visual features and differences discussed in this section between L2B and UHR wind estimates show some of the potential benefit of using UHR data. It is difficult, however, to quantitatively analyze the resolution difference or identify the noise content just from looking at these images. These issues are better investigated by looking at the spectrum of the winds, as well as other statistical properties. Such analysis requires that data be collected and averaged on a large scale.

3.2 Global and Regional Averaging

In order to analyze the spectral properties of ASCAT ocean winds, data are gathered from five different ocean regions over an entire year. Land causes discontinuities in the data, as well as contamination of wind data that is very close to land. For this reason, the regions are chosen to minimize the presence of land, so that as much continuous ocean wind data as possible is represented.

The regions chosen are rectangular regions in the major oceans. They are: North Atlantic, South Atlantic, North Pacific, South Pacific, and Indian. The coverage of each

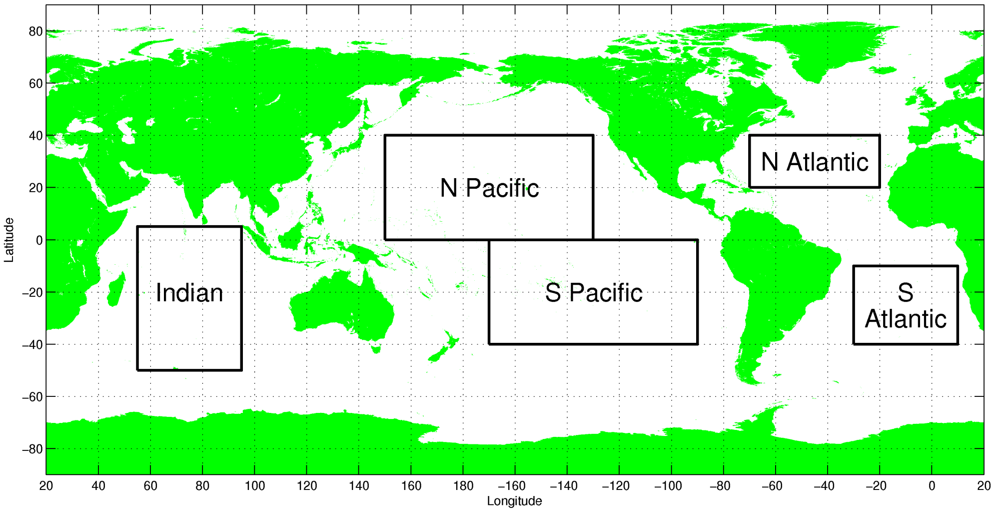

Figure 3.4: Regions used for averaging ASCAT data for statistical and spectral studies.

region is shown in Figure 3.4. Data from all the regions is averaged together to get global characteristics, and each region is examined separately to analyze differences in wind behavior between regions. Data is also divided in time, allowing comparison of behavior from different months or seasons. Both season and region affect weather, and these divisions may isolate similar data, such as more frequent storms, which could have an effect on the large scale data characteristics. The following sections contain studies of the overall statistical and spectral characteristics of ASCAT L2B and UHR winds, as well as case studies for several regions and time divisions.

3.3 Overall Characteristics

As discussed in Chapter 2, ocean winds are expected to have a red spectrum following a power law, meaning that the magnitude decreases as a constant power of spatial frequency. The rate of decay is referred to as the spectral slope because when represented on a log-log scale, it is ideally a line with constant slope. For ocean winds, this slope is generally about $k^{-5/3}$, with k being the spatial frequency, or wavenumber [4, 5].

An averaged periodogram representing the zonal and meridional spectra of global UHR and L2B winds for the year 2011 is shown in Figure 3.5, along with a $k^{-5/3}$ line for reference. The L2B spectrum approximates this reference slope, with a possible noise floor appearing to occur at about $\lambda = 30$ km.

The UHR spectrum extends further due to its higher sampling rate, but also shows a clear extension of a constant spectral slope out to at least $\lambda = 10$ km, after which noise may distort the data (see Appendix A for a discussion of noise floor effects). In this case there is not a clearly defined white noise floor. It appears that multiple levels of noise and filtering are introduced. An apparent first noise floor occurs at $\lambda = 10$ km, where the curve deviates from the $k^{-5/3}$ slope. After this the slope steepens again, but at $\lambda = 4$ km it flattens again. These may or may not both be actual noise floors but are referred to as such. Some of this deviation may be due to the UHR processing algorithm, as it involves gridding and averaging of measurements with irregular spacing and weighted averaging using an estimate of the SRF. Other likely causes of deviation are thermal noise and undersampling of the wind field. The winds are likely undersampled to some degree because an ideal $k^{-5/3}$ slope is not band limited and when sampled may cause aliasing that appears as noise (see Appendix A).

It is also possible that the area of the spectrum between the first and second noise floors contains at least some true wind information. While ocean winds are expected to approximate the $k^{-5/3}$ spectral slope, the energy cascade can sometimes be seen to include such an increase in this mesoscale range (see Section 2.1.1) [6]. Details of the spectrum at such high resolutions have not been definitively verified, however, as very few such data sets exist. Possible physical influences on high-resolution winds include the effects of three dimensional wind flow. Wind fields are typically approximated as two dimensional vector fields. This is reasonable because the width of the weather-containing atmosphere is usually insignificant compared to the resolution at which wind vectors are sampled. The troposphere, however, which contains nearly all weather and wind flow, extends to an average height of about 12 km [31]. At wavelengths smaller than this, three dimensional flow may be significant. This could have an effect on the observed two dimensional wind vectors and their spectrum.

A comparison between the L2B and UHR spectra suggests that UHR processing improves the effective resolution of ASCAT wind estimates by at least a factor of three (from 30 km to 10 km) based on the continuation of the power law behavior past what is seen in the L2B spectrum. The resolution may extend further to 3 or 4 km, depending on the

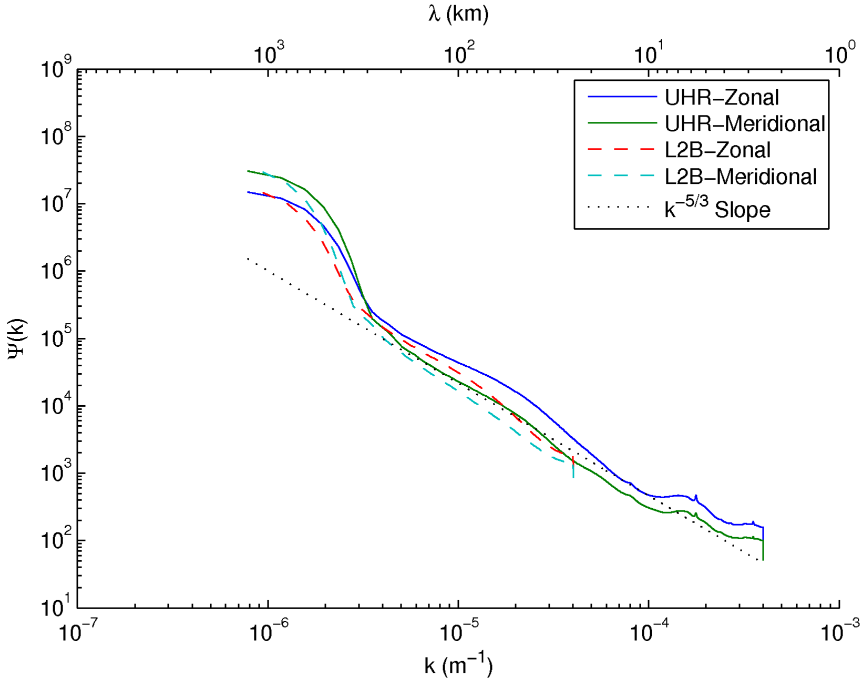

Figure 3.5: UHR and L2B spectra averaged over all regions for the year 2011. The L2B spectrum only extends to 25 km due to its course grid spacing.

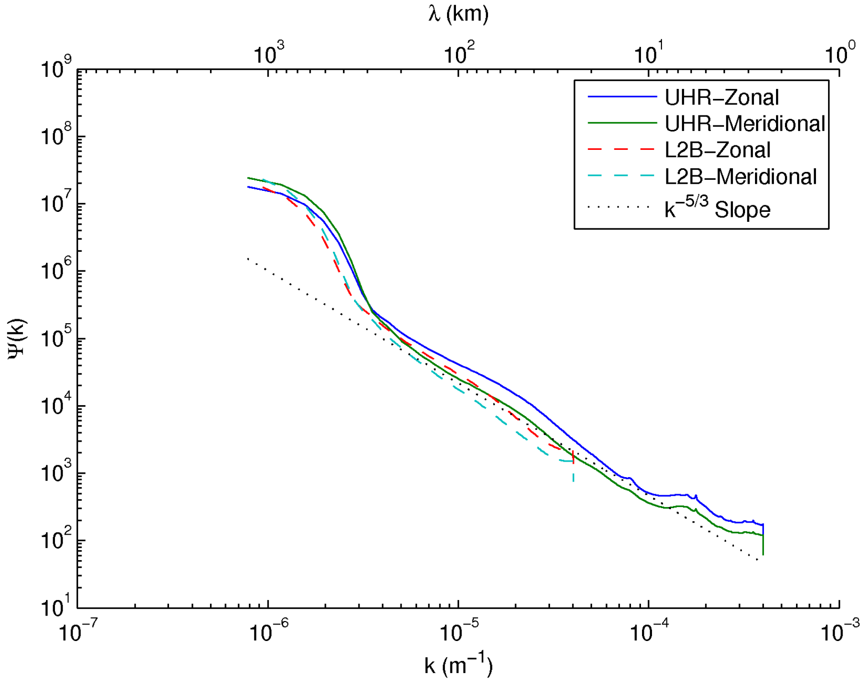

Figure 3.6: UHR and L2B spectra averaged over the North Atlantic region for the year 2011.

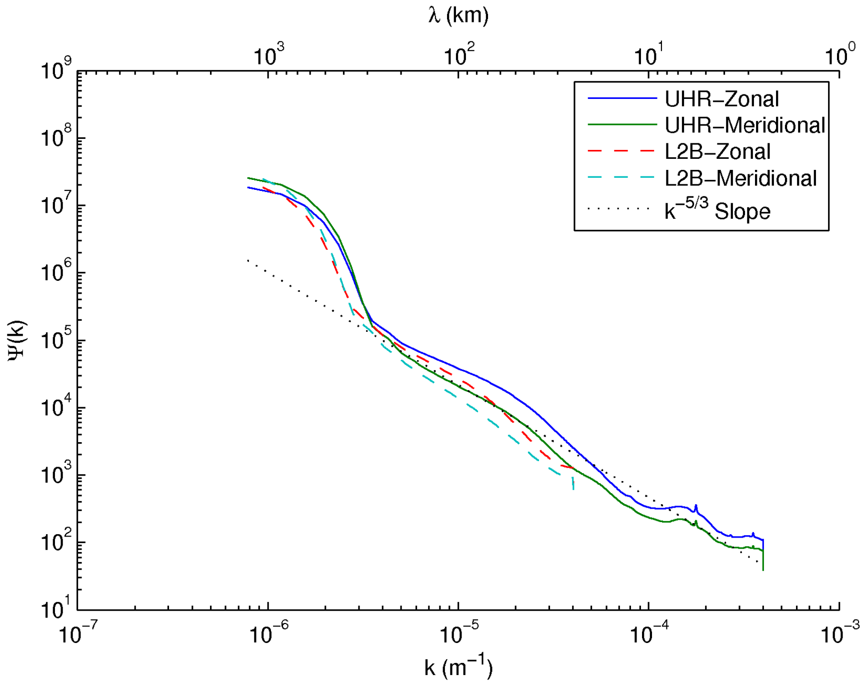

Figure 3.7: UHR and L2B spectra averaged over the South Atlantic region for the year 2011.

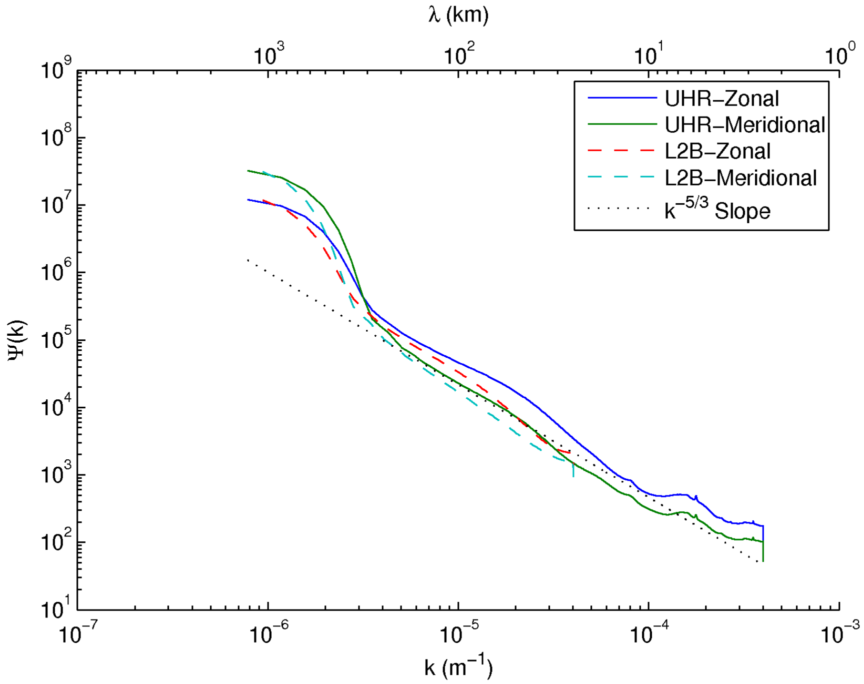

Figure 3.8: UHR and L2B spectra averaged over the North Pacific region for the year 2011.

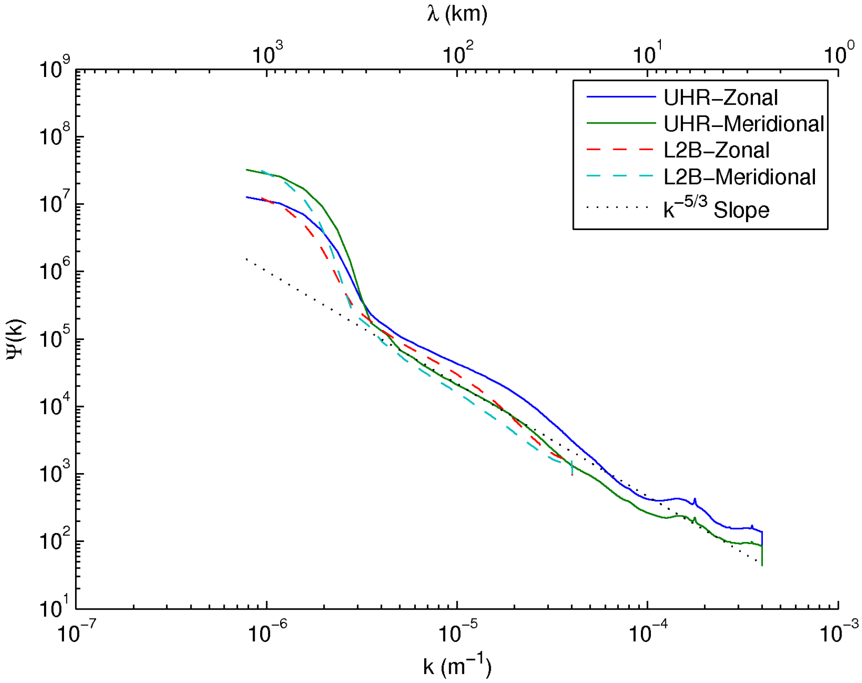

Figure 3.9: UHR and L2B spectra averaged over the South Pacific region for the year 2011.

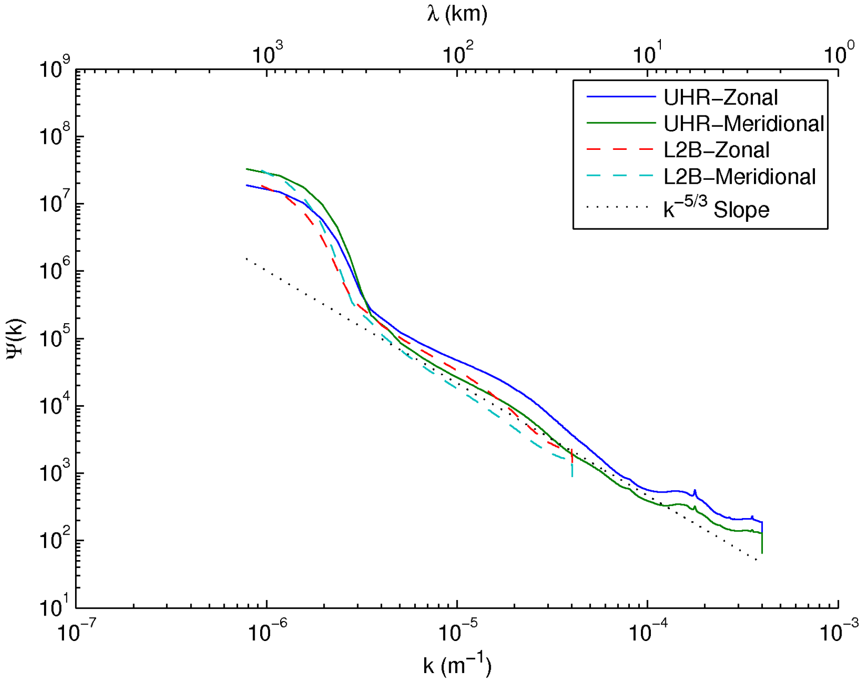

Figure 3.10: UHR and L2B spectra averaged over the Indian region for the year 2011.

true characteristics of the wind spectrum at these high wavenumbers and how they compare to the spectral deviation from the power law. The spectral behavior is not well known at high wavenumbers, but has previously been seen to include characteristics similar to those of the UHR spectrum [6].

3.4 Regional Analysis

A periodogram for each separate region is given in Figures 3.6 to 3.10. There are very few visible differences between the spectra of each region. The most noticeable difference is the presence of a small spike in the UHR spectrum at about $\lambda = 12.5$ km. This spike is more discernible in the North Atlantic and North Pacific spectra than in the others, and it is stronger in the zonal spectrum than in the meridional spectrum. It is unclear what this may mean, but it is interesting that 12.5 km is the spatial sampling rate of the L2B winds. The North Atlantic and Indian regions seem to follow the $k^{-5/3}$ slope best, and the South Atlantic region has a stronger dip at around $\lambda = 10$ km than the other regions.

This comparison of regional winds suggests that the ocean wind spectrum has little dependence on region, at least based on the regions chosen for this study. It also shows no evidence that the resolution of ASCAT UHR wind data is related to region, suggesting that UHR processing provides a global, high-resolution wind product.

3.5 Summary

Close analysis and comparison of ASCAT L2B and UHR wind estimates suggests that UHR winds contain high-resolution information that is not present in L2B winds. Visual comparison of the two data sets shows more clearly defined high-resolution features in UHR images. Wind speed contour lines are more detailed, and local maxima and minima in wind speed are sometimes more extreme. UHR processing also allows wind retrieval closer to land, and details of high-resolution wind events such as storms are more visible.

A spectral analysis shows that the $k^{-5/3}$ power law of the ASCAT wind spectrum is extended with UHR processing. This suggests that the additional high-resolution content present in UHR data may contain true wind data. However, the degree to which the resolution is extended is unclear. The high frequency part of the UHR spectrum deviates from the reference slope but then steepens and flattens again. It is unknown how much of this deviation is due to noise or if some is due to true wind characteristics, since the spectral properties of wind are not well known at such high frequencies. Similar deviations at mesoscale have been seen in some cases [6]. The spectral slope clearly extends to a wavelength of about $\lambda = 10$ km, and has a final apparent noise floor at about $\lambda = 4$ km. Either value is an improvement to the L2B resolution of 25 km, which has a noise floor at about 30 km.

Chapter 4

Validation of ASCAT UHR Using SAR Wind Data

Evidence has been presented that ASCAT UHR wind estimates contain high resolution information that is not present in the L2B winds. The next step is to validate the accuracy of this content. Unfortunately, there is no vector wind field truth data to compare it against. Instead, validation is performed by comparing to winds retrieved using synthetic aperture radar (SAR). SAR is a type of radar that is able to retrieve a backscatter signal of much higher resolution than that of scatterometers, making it a good candidate for validating high resolution data.

A complication with using SAR wind estimates is that it is much more difficult to determine wind direction using SAR data than it is using scatterometer data. This is why scatterometers are more widely used for wind vector retrieval. Because of this, a comparison with SAR can only involve the wind speed information. In order to allow the wind values to still be treated as vectors, the wind field is divided into its zonal and meridional components using direction information from other sources.

This chapter first provides basic background on SAR, especially in how it differs from scatterometry. The SAR product used to validate ASCAT UHR is then described. It is a satellite-based SAR on the European platform ENVISAT. The method for finding spatially and temporally collocated SAR and ASCAT data is then explained, following which a comparison is made between the two data sets using visual comparison, correlations, distributions, and spectra.

4.1 Synthetic Aperture Radar

Like scatterometers, SAR instruments are active remote sensors designed to transmit microwave pulses toward a surface and measure the reflected power, or backscatter. A σ^0

value is determined for the surface or target in question using the radar equation, as discussed in Section 2.2.

Scatterometers use a real aperture antenna to transmit and receive signals. The spatial resolution of the signal received from such an antenna is improved by increasing the size of the antenna, which decreases the beamwidth, causing a single pulse to illuminate a smaller area. SAR, on the other hand, takes advantage of the fact that radar instruments onboard an aircraft or satellite are constantly moving. The moving antenna is treated as an array of antennas, which allows a significant decrease in beamwidth, especially for small antennas. The resolution of a SAR instrument is increased by increasing the number of pulses that illuminate the same target location, or the dwell time of a single pulse on a given location. This is accomplished by increasing the beamwidth of the antenna, meaning that a smaller antenna will actually cause finer resolution when using SAR [1, 25].

As with scatterometers, wind vector estimates can be retrieved using the GMF and the retrieved SAR σ^0. However, it has already been mentioned that wind direction is not easily retrieved using SAR. In fact, wind direction is needed as an input to the GMF in order to determine the wind speed from SAR data, as SAR imagery is typically generated from only one look angle. These input wind directions are usually obtained in one of two ways. The first is from an outside source such as numerical weather models, and the second uses linear features in the SAR image itself. There are tradeoffs between these two methods. The linear features in the SAR images are not always present and may be affected by other atmospheric and oceanographic conditions, and model wind directions are usually at a much lower resolution than SAR data [8, 23, 24].

4.2 ENVISAT ASAR

UHR data is compared to wind estimates retrieved using data from the Advanced Synthetic Aperture Radar (ASAR), which is a SAR instrument that is part of the ESA's Environmental Satellite (ENVISAT) mission. ENVISAT is an Earth-observing satellite that includes many other remote sensing instruments used in environmental studies. The mission lasted from March 2002 to April 2012, providing nearly five years of overlap with ASCAT [32].

ASAR operates in the C band, as does ASCAT. It has several operational modes, which are designed for different functions and resolutions, as well as several polarization modes, including horizontal, vertical, and combinations of the two. There are numerous applications for ASAR data over oceans, land, snow, and ice. It can be used to study waves, coastal dynamics, ship traffic, vegetation, geology, urban areas, natural disasters, sea ice, and many other topics [32].

Wind speeds are not a typical product derived from ASAR data. However, ASAR wind estimates are acquired from the Alaska SAR Demonstration Project (AKDEMO), provided by the NOAA [33]. This data is retrieved on a 0.5 km grid, a pixel size less than half of that of ASCAT UHR. Additionally, the accuracy of SAR winds from this project was validated by Monaldo *et al.* through systematic comparison to National Data Buoy Center (NDBC) buoy wind speeds, model wind speeds, and QuikSCAT scatterometer wind speeds [23,24]. In these studies, the standard deviation of the difference with respect to SAR winds was found to be 1.76 m/s for buoy winds and 1.78 m/s for QuikSCAT winds.

4.3 Finding ASAR/ASCAT Collocations

A useful comparison of the ASAR and ASCAT wind estimates first requires finding collocations between the two data sets. Collocated data between the instruments exists when the their ground swaths illuminate the same surface location at the same time. The satellites carrying the ASAR and ASCAT instruments have different orbits, limiting the amount of data that can be used for direct comparison. Time stamps on the data files and latitude/longitude coordinates for the data points allow these collocations to be identified. Additionally, the AKDEMO does not provide wind estimates for all ASAR data, but instead provides only example wind fields, mostly focusing on certain near-coastal areas in North America (see Figure 4.1) [9]. This limits the number of collocations that can be found.

ASAR wind data files from the AKDEMO are found that overlap in space and are close in time to available ASCAT data. The criteria chosen for selecting these collocations are (1) less than a one hour time offset between ASAR and ASCAT data and (2) a spatial overlap of several degrees in both latitudinal and longitudinal directions. This analysis uses 105 such collocations between May 2010 and August 2011. The locations of these collocations

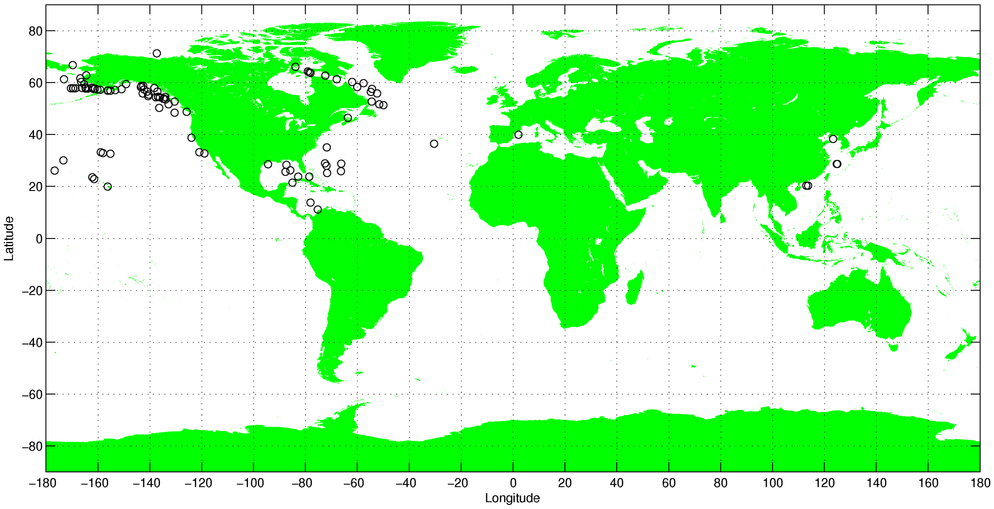

Figure 4.1: Locations of ASCAT/ASAR collocations.

are shown in Figure 4.1. One particular collocation represented in Figure 4.2 shows ASAR and ASCAT winds with a time offset of about 30 minutes and covering almost identical areas. With interesting visual features that encourage closer examination, this is a good example for visual inspection and comparison. Later in this chapter, all the collocations are used to obtain statistical and spectral data for a more quantitative analysis.

4.4 Visual Comparison

In Figure 4.2, there is a clear progression toward higher resolution moving from L2B to UHR to SAR. Similar low resolution features are visible in all three, which means that the data sets are consistent at low frequencies. It is unknown whether the high-resolution features and characteristics in the SAR and UHR winds are valid. They do, however, appear to be fairly consistent.

A good area for closer examination is the higher wind speed area in the bottom and left center of the field. While the L2B winds show little variation in these areas, the UHR winds show evidence of fine scale spatial wind speed changes. These variations appear consistent with those of the SAR image. A particular example is the area around 85 W and 24 N. Consider also the center of the wind field, where there is a transition between low and high wind speeds. This transition area has attributes and contour lines that are more

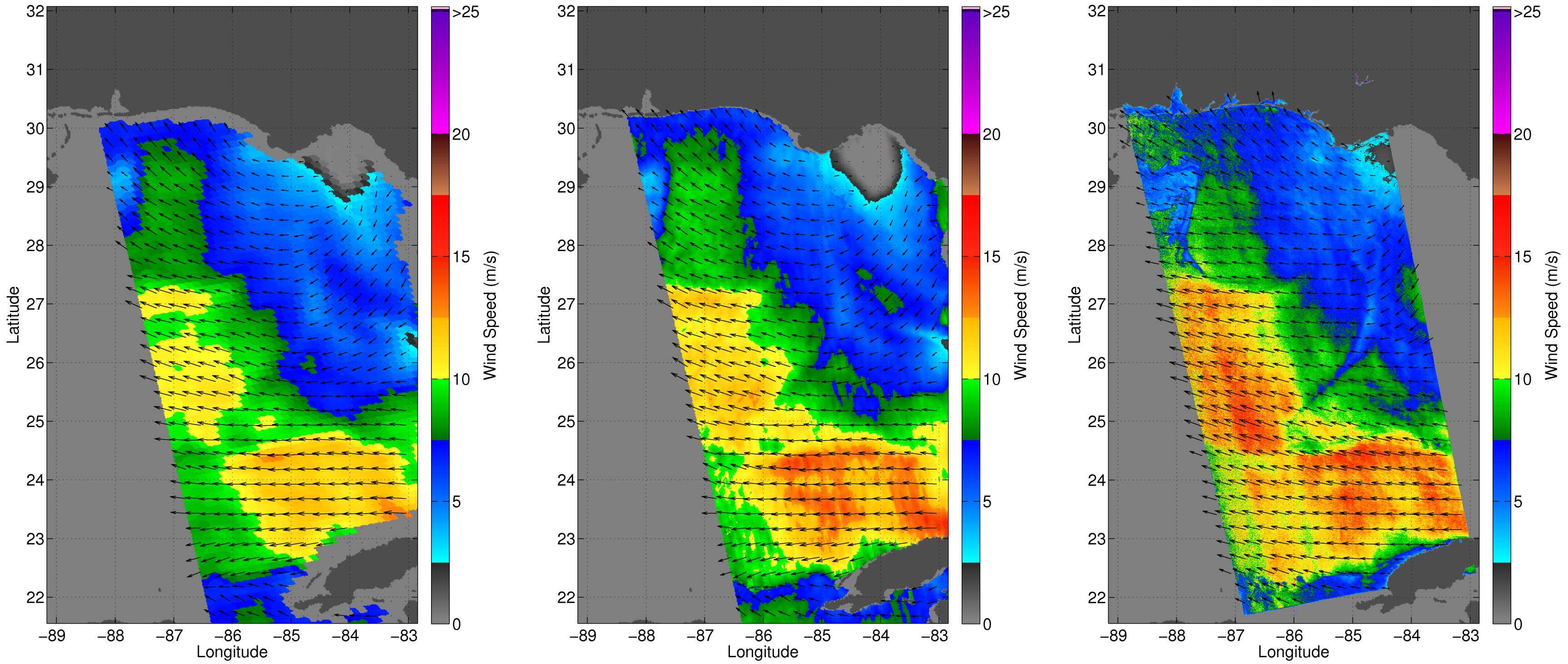

Figure 4.2: Collocated L2B (left), UHR (middle), and ASAR (right) winds retrieved on 5/15/2010 at 3:12:00 UTC (ASCAT) and 3:42:55 UTC (ASAR).

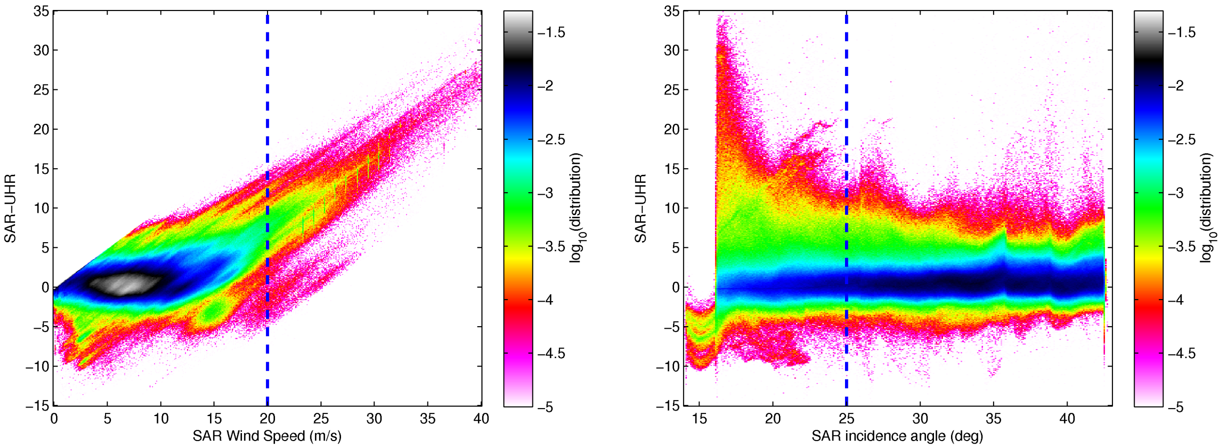

Figure 4.3: Two-dimensional histograms of ASAR wind speed (left) and ASAR incidence angle (right) vs ASAR/UHR wind speed difference. Used to determine cutoff values in order to reduce the high noise levels of ASAR winds that occur at high wind speeds and small incidence angles.

detailed in the UHR and SAR fields than in the L2B field. These details are similar across the two data sets, providing more evidence of the accuracy of the high-resolution winds in the UHR data set.

Visual comparison of these images builds the case that the added UHR resolution is accurate and consistent with the SAR data. However, as explained in Section 3.1, such analysis is not a rigorous validation, but a preliminary demonstration and a basis from which to pursue further analysis. Some of the especially high frequency variations in both the SAR and UHR images appear noisy. This appears as the apparent speckling effect in the SAR image and the rough look in the UHR image. For further analysis, statistical and spectral data are used to examine the wind estimates and determine the effects of noise and the consistency of the underlying data.

4.5 Distributions and Correlations

There are several important considerations when performing a statistical comparison of scatterometer and SAR winds. In remote sensing and wind retrieval, there is an inherent tradeoff between noise and resolution. We therefore expect UHR wind estimates to have greater noise content than L2B wind estimates, and SAR winds to be noisier then either of these. This may affect the statistics and spectra of these data sets.

Table 4.1: A statistical comparison of UHR, L2B, and ASAR wind speeds. Statistics are shown before and after excluding data outside the determined ranges for ASAR incidence angle and ASAR wind speed.

All Data	**ASAR**	**ASCAT UHR**	**ASCAT L2B**
Mean	8.561	7.377	7.314
Median	7.734	7.118	7.048
Std. Dev.	4.776	3.688	3.593
Within Range			
Mean	8.204	7.241	7.156
Median	7.693	7.044	6.914
Std. Dev.	3.842	3.635	3.530

It is mentioned in Section 3.1 that the accuracy of the GMF begins to degrade at high wind speeds. This affects SAR wind estimates as well. Additionally, the higher wind speeds may contain more noise and be affected by other fine scale oceanographic effects observed by SAR. While they are useful in observing the overall structure and visible features of a wind field, high wind speeds may adversely affect a statistical analysis of SAR winds.

Another consideration is the incidence angle of the SAR signal. ASCAT wind retrieval only uses data corresponding to incidence angles greater than 25°. ASAR wind estimates from the AKDEMO, however, correspond to incidence angles as low as 14°. It has been found in previous studies that at very low incidence angles, the expected inverse relationship between SAR incidence angle and σ^0 does not hold. This may cause both σ^0 and wind speed values to be lower than expected [23, 24]. A statistical analysis may be more useful if such data points are excluded.

Figure 4.3 contains histograms that illustrate these problems with high wind speeds and low incidence angles. The left plot is the joint distribution of ASAR wind speeds and the difference between ASAR and UHR wind speeds. It is clear that at high ASAR wind speeds the difference is much greater. A dotted line is shown at 20 m/s, above which all data points are excluded from further analysis. The right plot is the joint distribution of ASAR incidence angle and the ASAR/UHR wind speed difference. Again, it is clear that the data

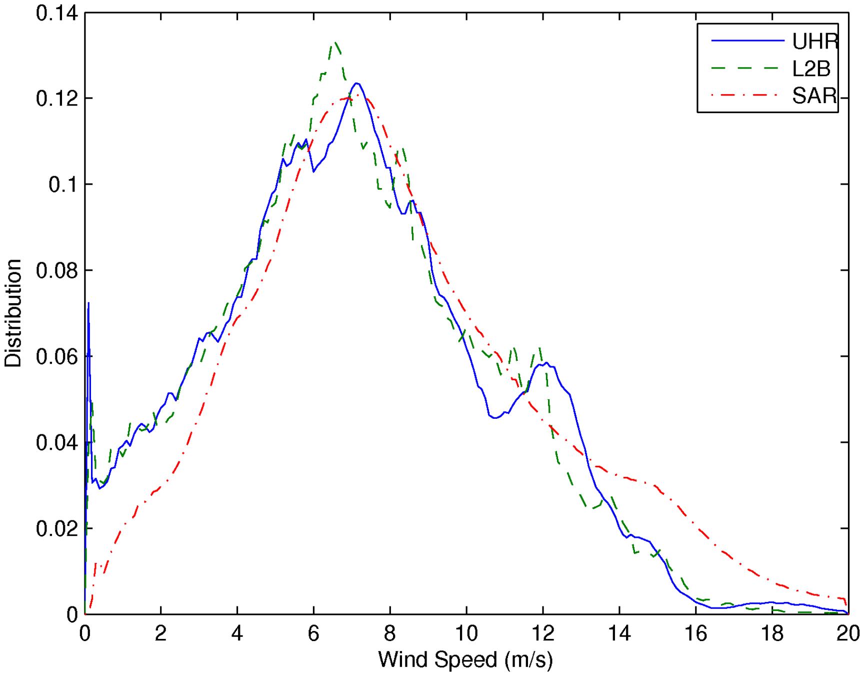

Figure 4.4: L2B, UHR, and ASAR wind speed distributions for all collocations, excluding data outside the determined ranges for ASAR incidence angle and ASAR wind speed.

sets are much less consistent at low incidence angles. The SAR wind speeds are too low at incidence angles between 14° and 16°, and below 25° the SAR/UHR difference distribution is more spread out and noisy. In this study, all data points with an ASAR incidence angle less than 25° are excluded from analysis. This cutoff corresponds to the ASCAT incidence angle range as well as that used in [23] and [24].

Statistics for the ASAR and ASCAT data sets are shown in Table 4.1, both before and after excluding data from outside the acceptable wind speed and incidence angle ranges. The biggest difference is in the standard deviation of the ASAR speeds. Before excluding out-of-range data, this value is unusually high, but afterwards it is much more comparable to ASCAT. Both the mean and standard deviation of the ASAR and ASCAT data sets become closer after the cutoff. It is also important to note that in all of these cases, the UHR values are closer to ASAR than the L2B values, suggesting that the high-resolution content in ASAR and UHR is compatible. The actual distributions are plotted for comparison in Figure 4.4. The ASAR distribution skews higher than the other two, as expected from the means in Table 4.1. The L2B distribution has a higher peak while the other two are more

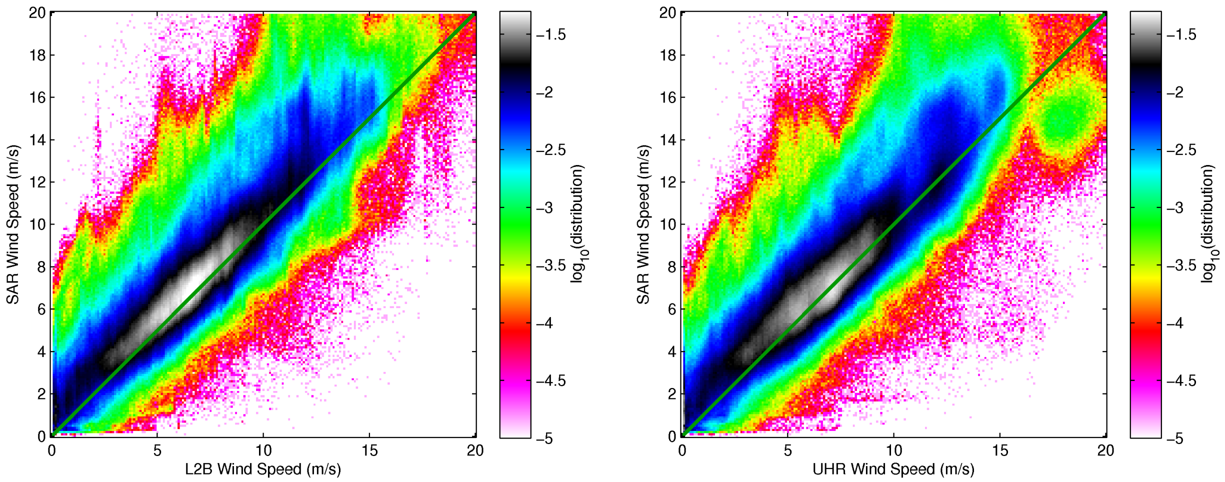

Figure 4.5: Two-dimensional distribution of ASCAT and ASAR wind speed values. ASAR winds are plotted vs. L2B winds (left) and UHR winds (right). A line with unit slope is plotted for reference. ASAR wind speeds > 20 m/s and incidence angles < 25° are excluded.

Table 4.2: A statistical comparison of how well UHR vs L2B wind speeds compare to ASAR wind speeds. ASAR wind speeds > 20 m/s and incidence angles < 25° are excluded.

Data Sets	Correlation Coef.	Std. Dev.	Mean Diff.
L2B/ASAR	0.898	1.992	1.048
UHR/ASAR	0.888	2.028	0.963

spread out, as expected from the higher standard deviation of the ASAR and UHR speeds. This again suggests that ASAR and UHR have more noise and higher resolution than L2B.

Figure 4.5 shows the L2B/ASAR and UHR/ASAR joint distributions, and their relative statistics are summarized in Table 4.2. Both distributions skew toward ASAR, matching the higher ASAR mean. This is more extreme at high wind speeds, suggesting either that these speeds are too high in ASAR winds, or that there is saturation in the ASCAT wind speeds. The correlation coefficient and standard deviation between L2B and ASAR are slightly better than those between UHR and ASAR, but the difference is small. It is promising that they have nearly the same correlation and difference when ASAR and UHR are compared on a much higher resolution grid than ASAR and L2B. It means that the added resolution does not degrade the correlation and provides evidence that the high resolution content of the two products agrees just as well as the low resolution content. The mean difference is better for UHR/ASAR than for L2B/ASAR, though again they are nearly the same. A slightly higher mean agrees with the visual observation UHR and ASAR winds show higher peaks in wind speed than L2B.

4.6 Spectrum

The statistical results discussed in the previous section relate to the comparison of individual wind vectors across the ASAR and ASCAT platforms, as well as overall mean difference and standard deviation. These comparisons do not address similarities and differences at different resolutions. A mean difference and a local, high-resolution difference are treated the same at a given grid point when performing a comparison using the correlation coefficient or standard deviation.

Comparing the spectra of the different data sets allows comparison based on resolution. This type of analysis can clarify and enhance some of the previous results, as well as provide new insights. Figure 4.6 shows the average wind speed spectrum for ASCAT L2B, ASCAT UHR, and ASAR winds over all collocations. They all have the similar overall trend of power law decay. However, there are significant differences which are more evident as the wavenumber increases in the log scale plot. The ASAR spectrum has the highest power at all resolutions. This agrees with the higher mean and standard deviation of the ASAR data set from Section 4.5, as well as the observations from the visual comparison in Section 4.4. At the smallest wavenumbers, the UHR power level is between ASAR and L2B, which is consistent with the fact that the mean wind speed increases from L2B to UHR to ASAR. As the wavenumber increases, however, the UHR power decreases more quickly than the ASAR power. While the UHR spectrum has a steeper slope, the shape is more constant. The ASAR spectral slope begins to change after the wavelength reaches about 30 km. It is impossible to know with certainty which is more correct, but there are likely positive and negative aspects of each.

The greater magnitude of the SAR wind spectrum in Figure 4.6, especially at high wavenumbers, may indicate that ASAR winds contain more high-resolution wind information than UHR winds. It may also indicate the the ASAR wind data contains more noise. Both of

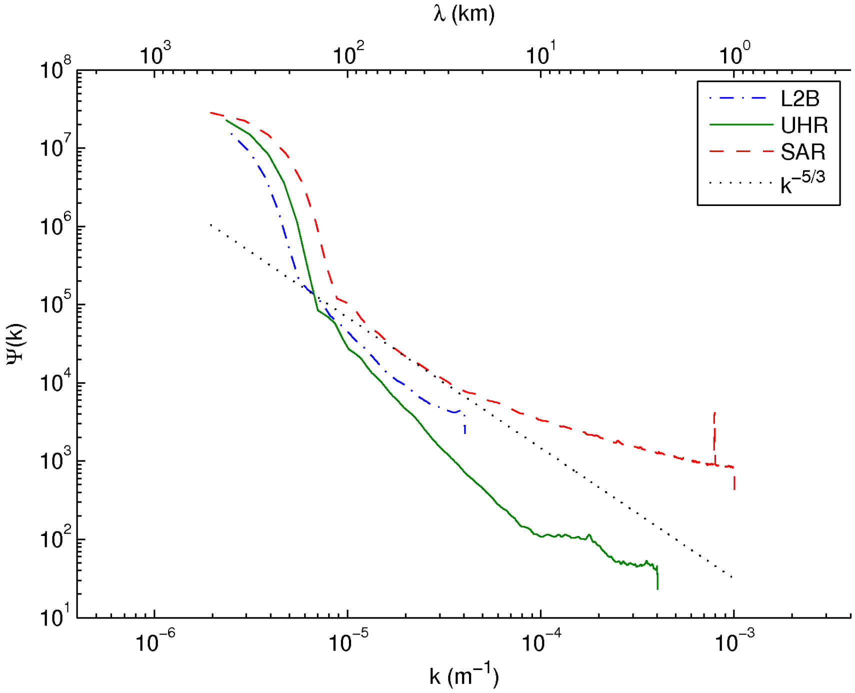

Figure 4.6: L2B, UHR, and ASAR wind speed spectra averaged over all collocations.

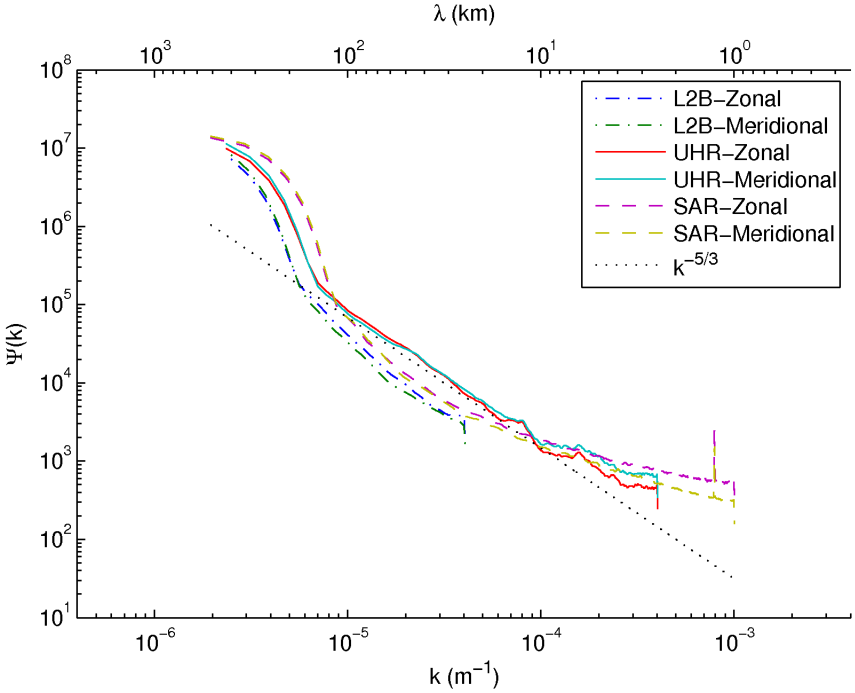

Figure 4.7: L2B, UHR, and ASAR zonal and meridional wind spectra averaged over all collocations.

these are likely true, as SAR winds are expected to have higher resolution than scatterometer winds, and the analyses in previous sections have suggested they are noisier. The change in slope indicates that noise may be a contributing factor, since a more constant slope is expected for the spectrum of ocean winds. The more constant spectral slope of the UHR winds is promising, though the lower power could indicate saturation of the ASCAT instrument at high wind speeds. This could also be caused by the windowing and irregular spatial averaging in the UHR wind retrieval process.

When direction information is added by generating the zonal and meridional spectra of each data set, there are significant changes. This is seen in Figure 4.7. All three spectra have much more similar power levels across all wavenumbers. The L2B spectrum stays essentially the same. The UHR spectrum, however, is raised in magnitude and follows the reference $k^{-5/3}$ slope closely until $k = 10^{-4}$ m^{-1}, or $\lambda = 10$ km. It is higher and more constant than the L2B spectrum. The changing ASAR slope stays about the same, but its magnitude is decreased, causing it to drop below the UHR spectrum for the mid-range wavenumbers and rise back above for the highest wavenumbers.

All the implications of these changes are not known, but the expected properties of the added direction information can help to explain them. SAR wind retrieval does not calculate wind direction. Instead it uses interpolated low resolution model wind directions as an input to the GMF. UHR winds, however, are scatterometer winds and do include wind direction at the same resolution as the wind speeds. Therefore, when combining wind speed and direction into zonal and meridional components, the UHR data uses two high-resolution data sets, while the ASAR data uses a high resolution and low resolution data set. This is a benefit of UHR winds, and including the direction information allows the analysis to show the true resolution content of the UHR data. The zonal and meridional spectra in Figure 4.7 suggest that after adding direction information the data sets are compatible, and the UHR data may have a spectrum that is more representative of expected ocean winds.

4.7 Vorticity and Divergence

A comparison of the vorticity and divergence fields for each wind data set may provide additional understanding and validation of UHR winds. Vorticity and divergence are derivative fields that provide additional information about ocean winds, as described in Section 2.1.2. The spectra of these fields are analyzed in order to compare the behavior at different wavenumbers.

An issue with comparing the derivative fields is that each data set is retrieved at a different grid resolution. If the derivatives are computed in all cases as first order differences, the difference will be taken across distances that do not match. The magnitude and behavior of the vorticity and divergence fields may vary based on the scale at which they are calculated. For this reason, the higher resolution data sets (UHR and SAR) are resampled at several different resolutions before calculating vorticity and divergence. Resampling is performed by averaging a group of pixels into one pixel based on the downsampling order. For example, downsampling by two involves dividing the grid into 2×2 sections and converting each section into one pixel whose value is the average of the four pixels.

The vorticity and divergence power spectra are shown in Figures 4.8 and 4.9. The results demonstrated in each of these figures are very similar. Each one shows the spectrum for each data set at various grid resolutions. As the order of downsampling for ASAR winds is increased, the spectrum approaches and then passes the power level for UHR winds. The UHR spectrum is located between the SAR spectrum sampled at 1.5 km and the SAR spectrum sampled at 2 km. This suggests the possibility that the resolution of the UHR winds is between these two values. This would correspond to an effective data resolution between 3 and 4 km. This matches the second deviation from the reference slope in the UHR wind spectrum, which is located at about $\lambda = 4$ km (see Section 3.3).

The UHR and SAR spectra match well when the vorticity and divergence are calculated at the same grid resolutions, as shown by the 5 km and 12.5 km lines in the figures. Both the power level and shape of the spectra are very similar, although there is evidence of sidelobes due to the spatial averaging performed when degrading the sampling resolution. Additionally, both the UHR and SAR spectra match the L2B spectrum at the 12.5 km grid resolution. These results validate the consistency of the derivative fields of all three data sets when analyzed at matching grid resolutions. This suggests that the data itself is consistent and that ASCAT UHR winds may provide valid high-resolution wind data down to a spatial resolution between 3 and 4 km.

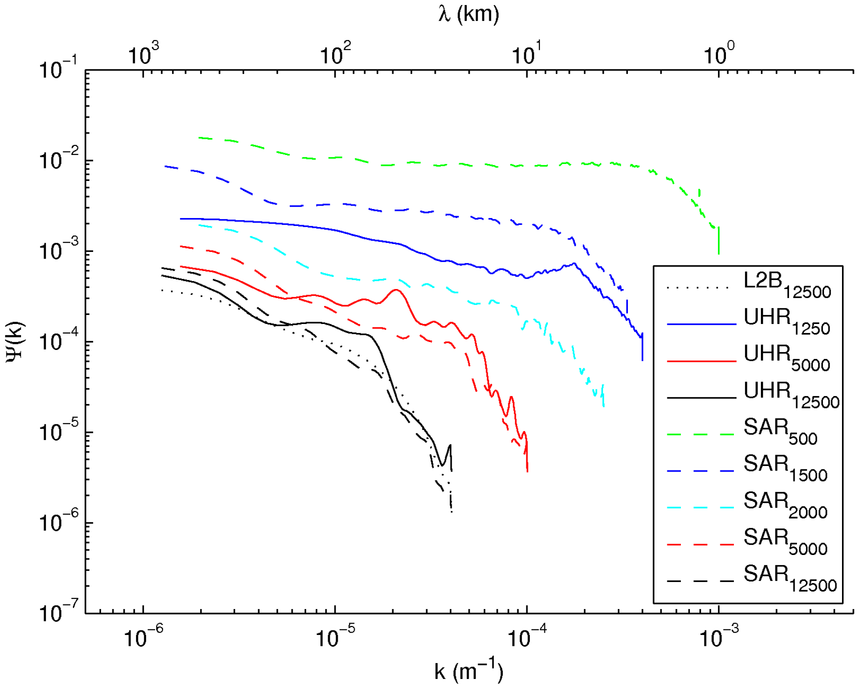

Figure 4.8: Vorticity spectrum for L2B, UHR, and ASAR winds. UHR and ASAR vorticity are computed at multiple resolutions. The subscripts in the legend indicate the pixel size in meters at which the vorticity was calculated.

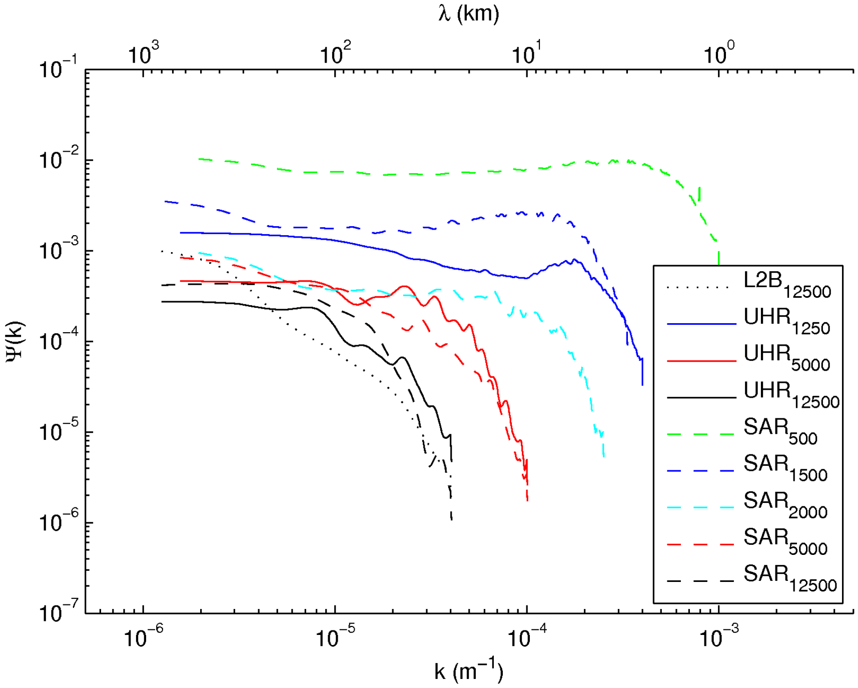

Figure 4.9: Divergence spectrum for L2B, UHR, and ASAR winds. UHR and ASAR divergence are computed at multiple resolutions. The subscripts in the legend indicate the pixel size in meters at which the divergence was calculated.

4.8 Summary

This comparative analysis of high-resolution ASCAT and ASAR wind data shows consistencies between the data sets, as well as problems that make it difficult to arrive at definitive results. A visual comparison of collocated wind fields shows a visible increase in resolution from ASCAT L2B to ASCAT UHR to ASAR winds. There are high-resolution features in both the UHR and ASAR winds that are not present in the L2B winds or are less pronounced. This includes higher peak values in high wind speed areas and more detailed transition areas between high and low speeds. The two high-resolution wind products also appear to contain more noise, as evidenced by the speckling and roughness in the images.

Statistical comparison of the data sets results in a high correlation coefficient of 0.888 between UHR and ASAR wind speeds, nearly the same as that between L2B and ASAR (0.898). The standard deviation between data sets is also comparable to L2B and ASAR. UHR and ASAR have a slightly smaller mean difference, though again nearly the same. It is positive that the statistics are so similar when ASAR and UHR are compared on a much higher resolution grid than ASAR and L2B. It gives evidence that the high resolution information of the data sets agrees just as well as the low resolution content. The ASAR and UHR products have higher individual standard deviations than L2B wind speeds, agreeing with the visual clues that they have a higher noise content. This suggests more noise, which reduces the correlation and makes comparison and validation more difficult.

Spectral analysis extends the comparison. The spectral slope of the ASAR wind changes to become more shallow at high wavenumbers, further indicating the presence of high-resolution content as well as noise. The UHR spectrum has a significantly lower magnitude and steeper slope than ASAR at high wavenumbers when only wind speed is included in the analysis. When direction information is included by calculating the spectra of the zonal and meridional components, the relative magnitudes of the spectra are closer. The magnitude of the UHR spectrum increases and follows a $k^{-5/3}$ slope closely up to a 10 km resolution, while the ASAR spectrum decreases slightly in magnitude. This helps to show the benefit of UHR winds in providing high-resolution direction information.

An analysis of vorticity and divergence gives more evidence of the consistency between ASCAT UHR and ASAR wind estimates, further validating the high-resolution wind content present in the UHR data. This comparison is performed by calculating vorticity and divergence at similar grid resolutions for each data set. The UHR results are most similar to the SAR results at a resolution between 3 and 4 km, which is near where the second noise floor of the UHR wind spectrum is located. When the vorticity and divergence are calculated at exactly the same grid resolution for UHR, L2B, and ASAR winds, the spectra match very well.

Due to the lack of truth data, it is impossible to precisely quantify the accuracy of either ASCAT or ASAR winds. The consistency of the high-resolution features in the data sets suggests that they do contain useful high-resolution content, and that UHR processing increases the resolution of ASCAT winds from what is contained in the L2B data set. Statistics show that all of the products are correlated, though the high-resolution data is noisy. It appears that the UHR wind data have a spectrum indicative of what is expected from ocean winds to at least a 10 km resolution. These results suggest that ASCAT UHR winds represent a valid high-resolution wind product that can be used with care in applications that need such additional resolution.

Chapter 5

Improving ASCAT UHR Wind Retrieval

In the previous two chapters, ASCAT UHR wind estimates are analyzed and validated. With limited truth data, it is impossible to determine the true accuracy and noise content of the UHR wind vectors. Nonetheless, It is determined that the high-resolution content in this data set appears useful. The UHR spectral slope is extended from what is seen in the L2B data, and many high-resolution features match what is seen in high-resolution SAR winds.

Careful examination suggests some issues with the data, including multiple noise sources, possible saturation at high wind speeds, and inaccuracy at low wind speeds. This chapter explores counteracting these problems using model-based improvement of ambiguity selection.

First, common issues in scatterometer wind data are summarized. Then, the current ASCAT UHR ambiguity selection process is described. The effects of ambiguity selection errors on wind quality and spectrum are then investigated, following which a data-derived wind model is developed and used to find errors in ambiguity selection and correct them. The results of this process are compared to the results of using a simple median filter on the original UHR wind field, and the effects on the quality of the wind product are considered.

5.1 Noise and Inaccuracy in Scatterometer Winds

Noise and inaccuracies may be introduced at many points in the process of scatterometer wind retrieval. These have been mentioned and discussed in Chapter 2 and throughout this thesis. They are summarized here for convenience.

Atmospheric phenomena may affect the microwave backscatter, yet are not directly related to the wind velocity. Rain especially is known to adversely affect wind retrieval, and there may be other unknown or less significant variables, such as temperature.

The GMF may only be accurate over a limited range of wind speeds. For example, the GMF may not hold at low wind speeds because the wind speed must reach a certain point before having enough traction with the ocean surface to actually cause such waves [34]. At high wind speeds, the GMF may saturate.

Additionally, the frequency band used by the scatterometer may affect sensitivity to certain wind speeds because of a difference between signal wavelength and water wavelength, and the scatterometer instrument itself adds thermal noise as it measures backscatter, degrading the SNR.

Other possible noise and inaccuracies come from the data processing. ASCAT UHR processing in particular involves gridding and averaging of measurements with irregular spacing, as well as windowing and weighted averaging using an estimate of the SRF. After this main processing is finished, there is still the issue of ambiguity removal. Each grid point in a wind field can have multiple possible vectors with equal probability according to the GMF. The ambiguity removal step must choose which of these vectors is the most accurate and self consistent with the rest of the field. This is difficult to accomplish, and there are various methods, causing it to be another source of inaccuracy.

5.2 ASCAT Ambiguity Selection

Improvement of ASCAT UHR ambiguity selection is a good candidate for reducing noise and inaccuracies in the wind product. Ambiguity selection has been a frequent subject of studies of scatterometer wind quality and improvement [3, 12, 35, 36]. It is important, however, to first understand the specific ambiguity selection algorithm for ASCAT. The ASCAT product guide [16] describes the ambiguity selection process used for ASCAT L2B winds as follows:

> "A wind direction ambiguity removal step is further applied, based on variational meteorological analysis and relying on prior numerical weather prediction (NWP) model information. In 2D-VAR a cost function is minimised. The cost function

> is formulated in terms of wind increments and penalises deviations from both a background wind field and the ambiguous scatterometer wind solutions obtained from scatterometer wind retrieval."

This is a typical ambiguity selection algorithm that minimizes a cost function using NWP model winds and self-consistency within the retrieved wind vectors. This description is specific to the L2B product, while ambiguity selection for UHR is more simple. It consists of choosing the ambiguity closest in the L^2 norm to the interpolated L2B wind vector. This is a simple solution that should be quite accurate, but inaccuracies and inconsistencies in the wind field may remain due to the presence of fine scale variations. The following sections discuss the potential impact of such errors, and present a model-based ambiguity selection process that extends this preliminary solution and reduces errors.

5.3 Preliminary Spectral Analysis

A possible way to analyze the effect of ambiguity selection errors on wind field quality is to examine their effect on the spectrum. Ocean winds are known to have a one-dimensional wavenumber power spectrum that follows the power law with an approximate slope of $k^{-5/3}$. In this thesis, UHR winds have been shown to follow this rule fairly well, with the exception of variations at the highest wavenumbers. These variations can most likely be attributed to the noise and inaccuracies discussed in Section 5.1. This section investigates whether errors in ambiguity selection may cause or add to this variation from a constant spectral slope.

A simple analysis of the effect of ambiguity selection on the wind spectrum is done by purposefully choosing incorrect ambiguities for some of the wind vectors and observing how the spectrum is affected. Three levels of ambiguity changes are analyzed. First, the same ambiguity number is chosen for all wind vectors. This may at times coincide with the correct ambiguity selection, but causes many to be incorrect. This is the "all bad" case. Next, the same ambiguity is similarly chosen, but for only a small strip of the wind field. This is the "bad strip" case. Last, only two "bad" ambiguities in each row of wind vectors are chosen. This is the "two bad values" case. Figure 5.1 shows the averaged periodogram for one month of data for each of these cases in the North Atlantic region. Figure 5.2 illustrates each case and how the ambiguities are changed. The spectra in Figure 5.1 show that this type of

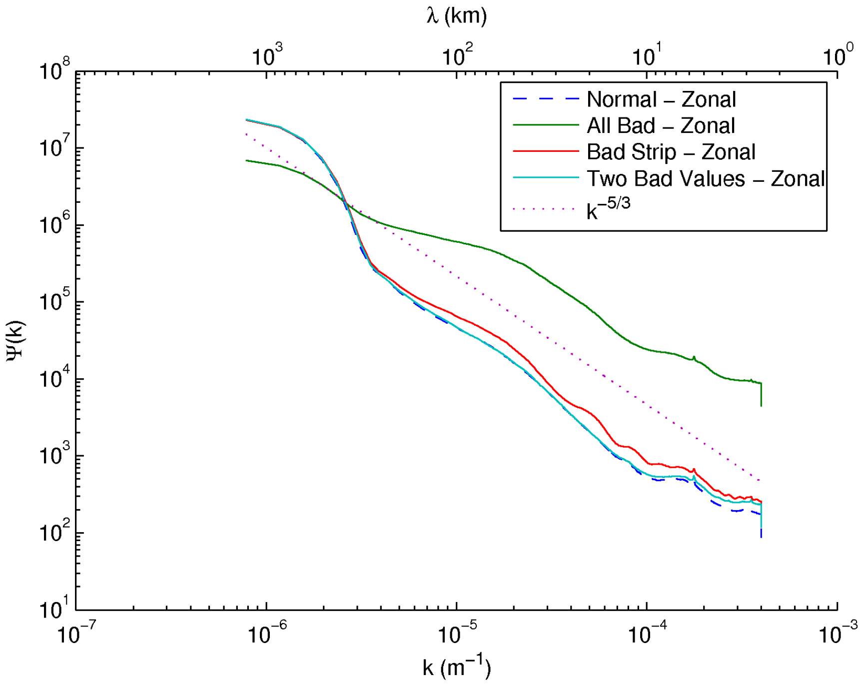

Figure 5.1: Spectra for wind fields with different levels of changed ambiguities. Data is averaged over one month in the North Atlantic region.

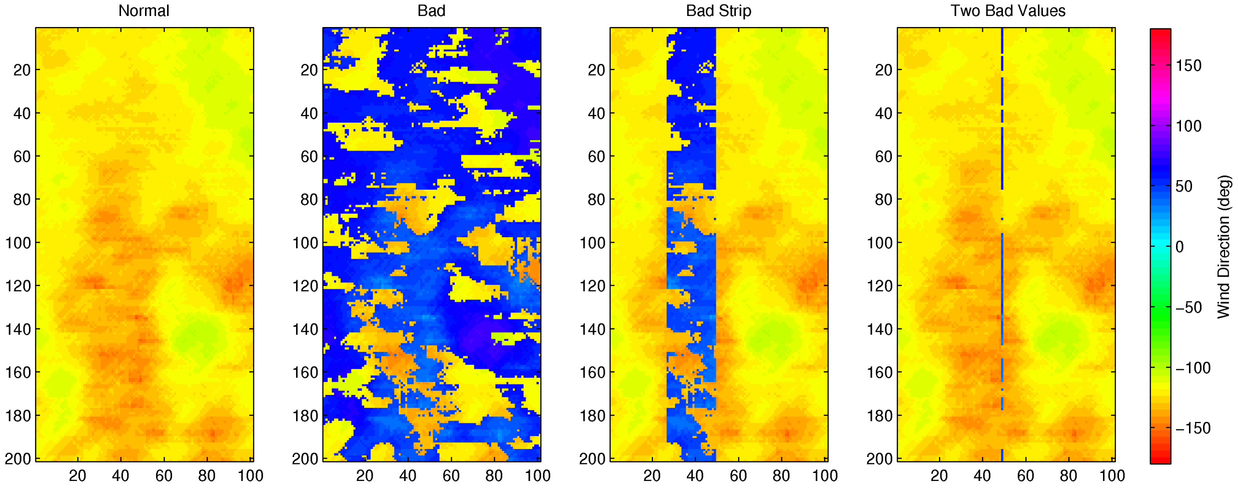

Figure 5.2: Illustration of how different amounts of ambiguities are changed in the wind fields to analyze the effect on the spectrum. The wind direction field is shown.

change in ambiguity selection is essentially like adding white noise, although the “bad strip” case also adds sidelobes due to the fact that making it a strip is like adding a rect function. The more bad ambiguities are selected, though, the higher the noise floor is raised.

It is unclear from this initial analysis if ambiguity errors contribute to the spectral deviations from a $k^{-5/3}$ slope at high wavenumbers. Adding ambiguity errors does raise the noise floor at these high wavenumbers, however, warranting further investigation into the actual ambiguity errors present in UHR data. A model-based method for finding and correcting possible ambiguity errors is presented in the following section, after which the effect of these corrections on the spectrum is examined.

5.4 Ambiguity Errors and Correction

In order to identify and correct potential ambiguity selection errors in ASCAT UHR wind vectors, a wind field model is created based on ASCAT data in order to create a field that is self-consistent [12, 35–37]. The ambiguity that is closest to the model vector for a given location is considered the “correct” ambiguity and ambiguity errors are selections that do not fit this criterion.

5.4.1 Wind Field Model

A linear model is used to characterize the wind vectors, adapted from the process used by Gonzales and Long [35]. Such a model can be expressed as

$$\mathbf{W} = \mathbf{F}\mathbf{X},$$

where $\mathbf{X}$ is a vector containing the model parameters and $\mathbf{F}$ is a model matrix whose columns form a basis set for possible wind fields. $\mathbf{W}$ is a row scanned vector of the u and v components of a sampled wind field. The model used is the Karhunen-Loève (KL) model, in which $\mathbf{F}$ is derived from the eigenvectors of the autocorrelation matrix $\mathbf{R}$ of the sampled wind field. $\mathbf{R}$ is defined as $E[\mathbf{W}\mathbf{W}^T]$. The true $\mathbf{R}$ is not known, so it is estimated from the sample autocorrelation of one month of UHR data in the North Atlantic. Different seasons and

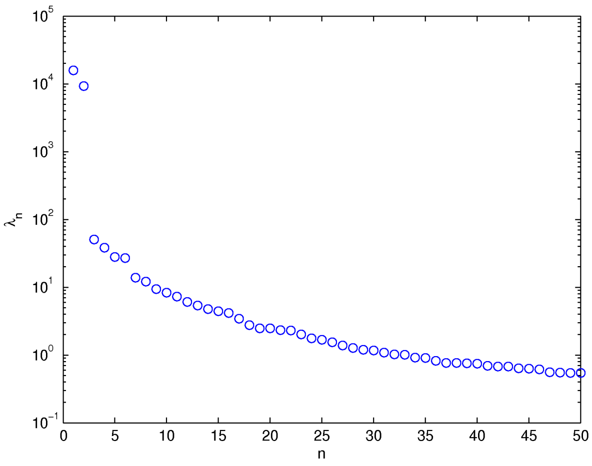

Figure 5.3: First 50 eigenvalues in the KL model.

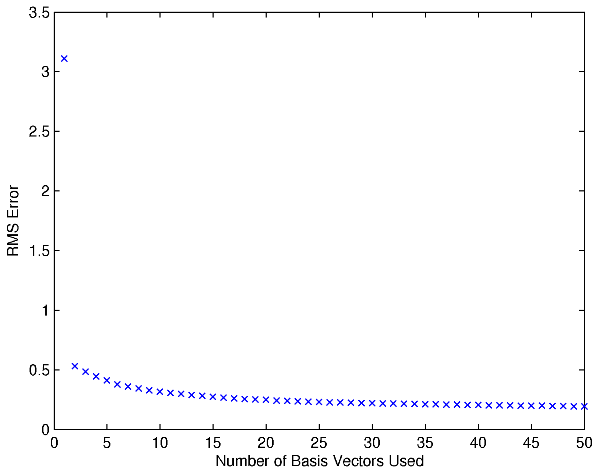

Figure 5.4: RMS error based on the number of basis vectors being used in the wind model.

regions may have slightly different correlation matrices, but testing shows they do not have significantly different results in finding and correcting ambiguity errors.

The **W** vectors used are taken from 18 × 18 wind vector regions that overlap by 50% in both directions. These regions are relatively small, since each ASCAT swath has a width of about 440 UHR wind vector cells. A single UHR rev file with very little land, for example, contains over 20,000 regions. However, the regions are constrained in size to allow a reasonable processing time. A size of 18 is subjectively chosen based on a tradeoff between processing time and data extent. With an 18 × 18 region, each vector has 648 elements, and the one month of North Atlantic wind data used in the analysis includes 2,353,748 such regions. Figure 5.3 shows the first 50 eigenvalues of the estimated autocorrelation matrix, and Figure 5.4 shows the RMS error between the retrieved wind field and the model wind field based on the number of eigenvectors used in the model to form the matrix **F**. These values are used to subjectively choose the number of basis vectors used in the model, accounting for a tradeoff between better modeling and inclusion of high-resolution information, and finding ambiguity errors. The number of basis vectors chosen for the model is 64, which is about a tenth of the eigenvectors of the 648 × 648 matrix **R**, and is sufficiently past the area where the two graphs taper off significantly.

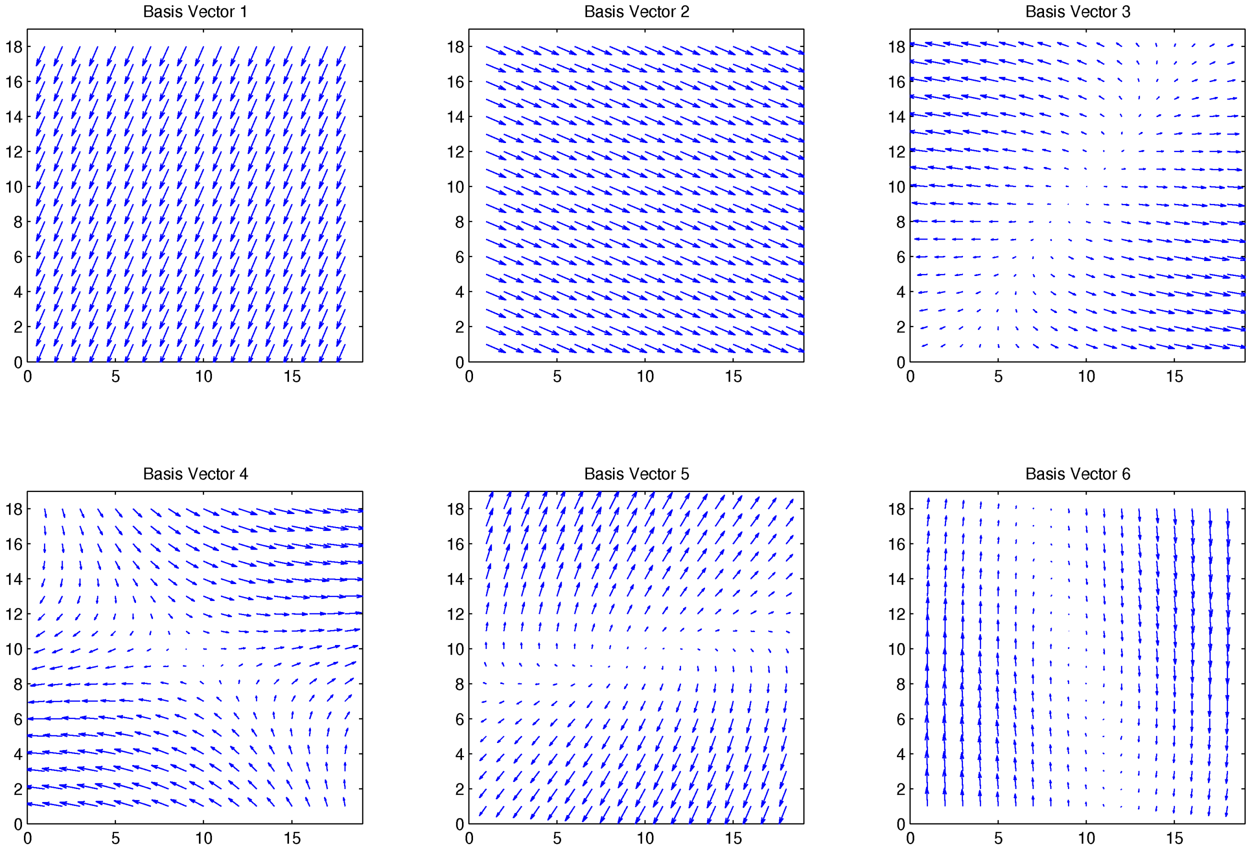

Figure 5.5: First six basis vectors of the KL model.

The first six basis vectors of the model are shown in Figure 5.5. These are important because they represent the most common wind field components, and the corresponding eigenvalues are larger for these than the remaining eigenvectors (see Figure 5.3). The first two basis vectors represent linear wind fields, and the others represent converging winds, diverging winds, and saddle points. The best linear fit of all the basis vectors is used to find a model representation of each 18×18 wind vector region. Model errors are then calculated and possible ambiguity errors are found.

5.4.2 Errors

After a retrieved region of wind vectors is fitted to the model, all the ambiguities for each wind vector are examined, and the closest ambiguity in the vector sense (using the L^2 norm) to the model vector is selected as the correct ambiguity. If this is different than

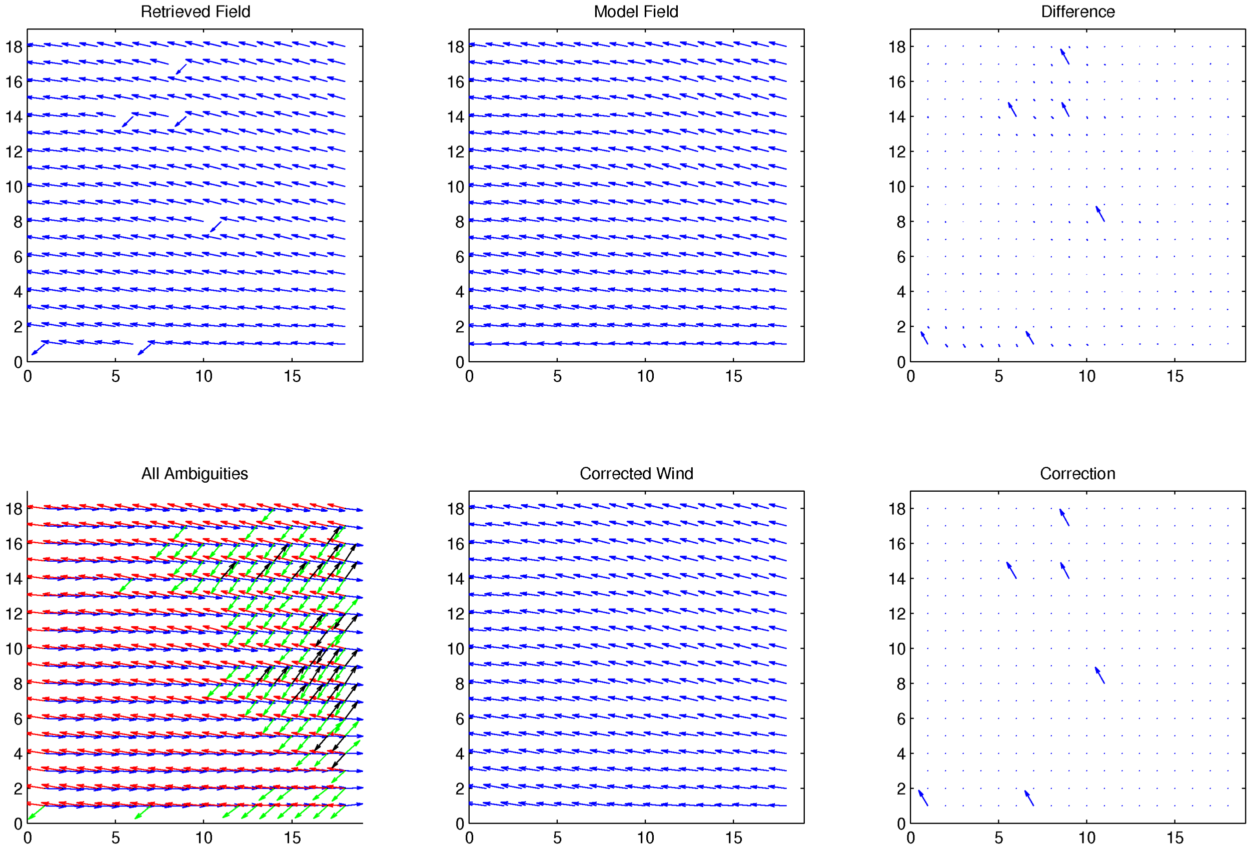

Figure 5.6: Illustration of the process of correcting ambiguity selection errors using model fitting. Top row: original retrieved UHR winds, model fit, difference field. Bottom row: All ambiguities overlaid in separate colors, ambiguities closest to the model field, corrections.

the originally chosen ambiguity, a possible ambiguity error has been found. This process is illustrated in Figure 5.6 with a region that contains clear examples of ambiguity selection errors. Visually, it appears that six of the vectors in the wind field are incorrect, because they are discontinuous with the surrounding vectors. The model fit supports this, producing a nearly linear field with none of the discontinuities. Upon examining all ambiguities for each wind vector, it is found that there are unused ambiguities which allow the retrieved field to better fit the model field.

Some wind fields, however, are much more difficult to model. In these cases, it is unclear if found errors are truly ambiguity errors or if they are the result of noise or modeling error. One such example is shown in Figure 5.7. There are many apparent discontinuities and ambiguity errors in this field, so many that it is hard to know if the model actually

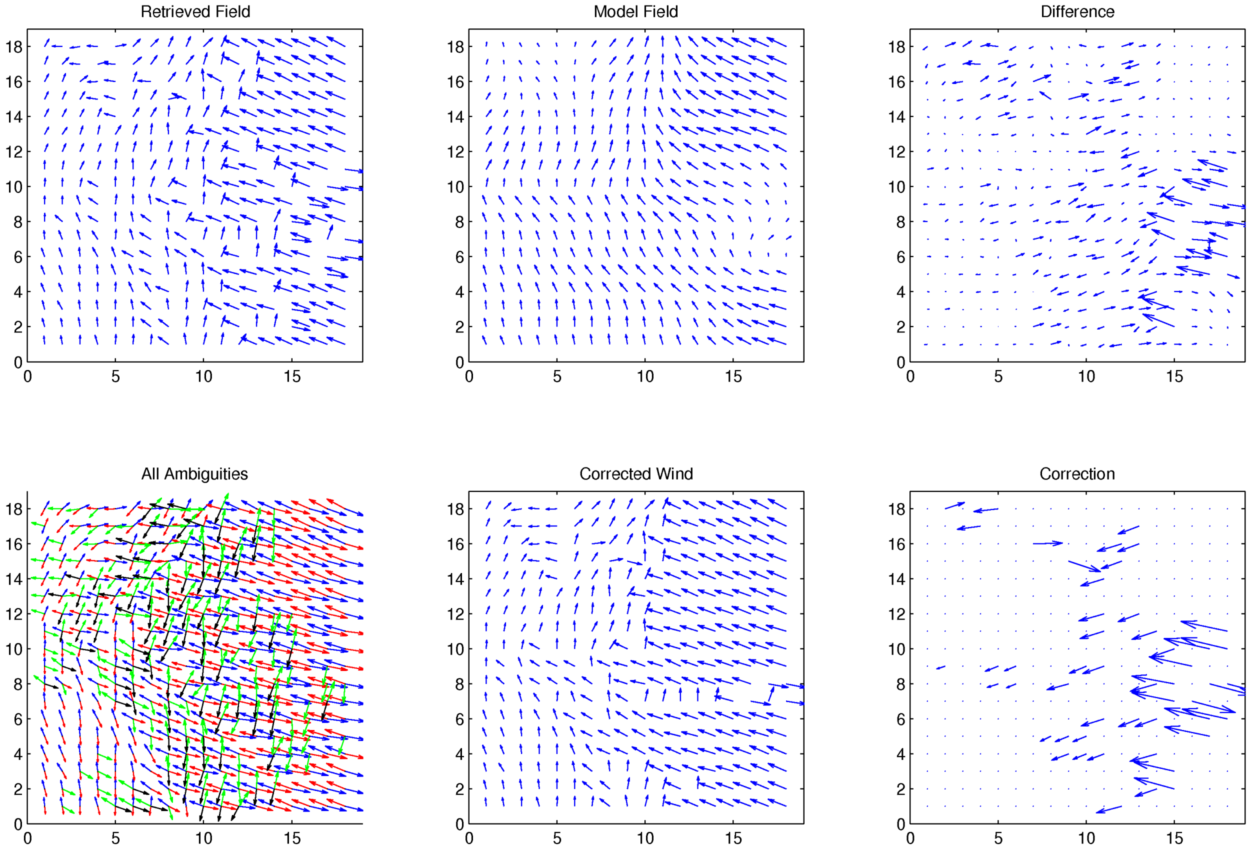

Figure 5.7: Correction process for a field that is difficult to model.

captures the true behavior. The corrected field looks a little more self-consistent, but still has discontinuous transitions from one wind direction to another. Cases such as this often arise when they are on the border of a wind front or a storm, which is hard to model because it naturally has properties that are close to being discontinuous.

Modeling error can also occur in cases of low wind speeds. The C-band signal used on ASCAT is not as sensitive to low wind speeds as it is to high wind speeds, and low wind speeds are also more sensitive to noise since they correspond to a lower signal strength. Figure 5.8 shows the percent of the total regions that are above a certain threshold in ambiguity errors and normalized RMS error. It is clear that the percent of regions with error is high for low wind speeds. There seem to be two boundary speeds: one at about 7 m/s, and one at about 2 m/s. Below these speeds the error likelihood increases greatly.

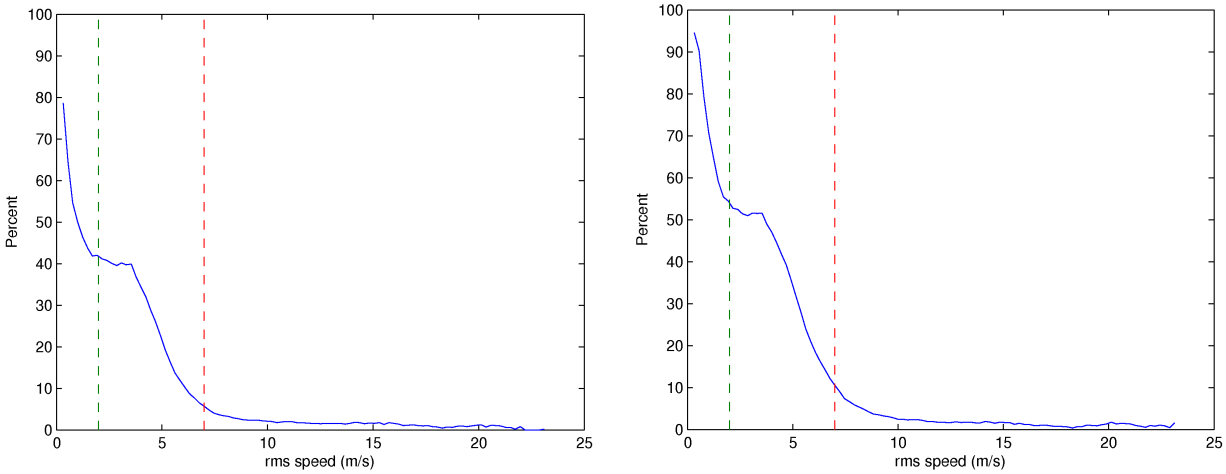

Figure 5.8: Percent of total regions that have at least one ambiguity error (left) and a normalized RMS error > 0.05 (right) at different RMS wind speeds. The dashed lines are at 2 m/s and 7 m/s, and show two cutoff points below which percent error increases rapidly.

Whatever their cause, errors caused by noise and modeling error may cause ambiguity errors to be found that are not true ambiguity errors. This is a problem with this type of ambiguity correction. However, in general, the corrections still produce a more self-consistent field, which may still have benefits in the wind product.

5.5 Spectrum

The effects of the ambiguity correction on the wavenumber spectrum of the wind field are analyzed in reference to the spectral properties of ASCAT UHR winds that are discussed in Chapters 3 and 4 and reviewed in this chapter. Specifically, it is considered if correcting errors in ambiguity selection affects the spectrum in a way that reduces variation from a constant $k^{-5/3}$ spectral slope at high spatial frequencies.

Figure 5.9 shows average spectral data over the month of North Atlantic wind data that is used in this study. It shows the spectrum for the original retrieved wind, the model wind, the corrected wind, and the original wind field after being filtered with a 3×3 median filter. A dotted line is also given as a reference $k^{-5/3}$ spectrum. The ambiguity correction in this study appears to at least lessen the high-frequency variations and bring the spectrum closer to the reference slope. The wind model has a more extreme effect and brings the spectrum down below the reference. This is to be expected however, as the model only

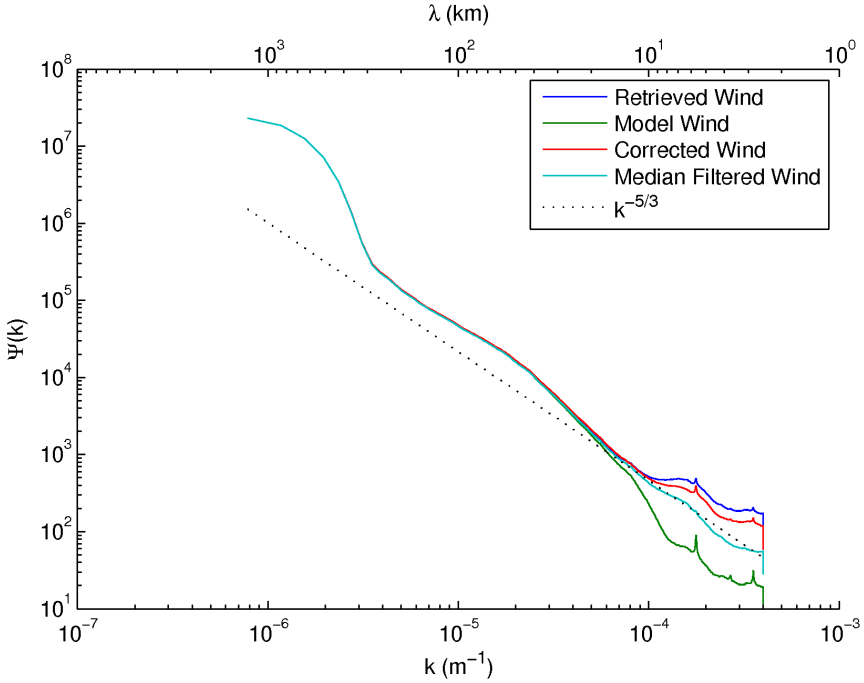

Figure 5.9: Average zonal spectrum of the original retrieved UHR wind field (blue), the model fit of the wind field (green), the wind field with corrected ambiguity errors (red), and original UHR wind after median filtering (cyan).

includes the most important basis vectors and thus essentially has a low-pass filter effect. Figure 5.10 shows the differences from the original wind field for both the model and the corrected wind.

The median filtered wind spectrum is provided in both plots in order to determine how similar this process is to simply applying a median filter in order to get rid of the outliers and discontinuities. A median filter is a less complex and computationally intensive procedure than the model-matching process, so if it produces similar results it may be preferable. The resulting spectrum is changed in a similar manner to the other two, and is between them in the magnitude of the difference. It results in a more constant slope than the ambiguity correction, but this slope may be too steep, showing more similarities to a low pass filter, like the model spectrum. It significantly reduces the deviation from $k^{-5/3}$ at high frequencies, and may warrant further investigation as a viable option for wind correction. The benefit of ambiguity correction, though, is that it keeps an actual retrieved value for each wind vector.

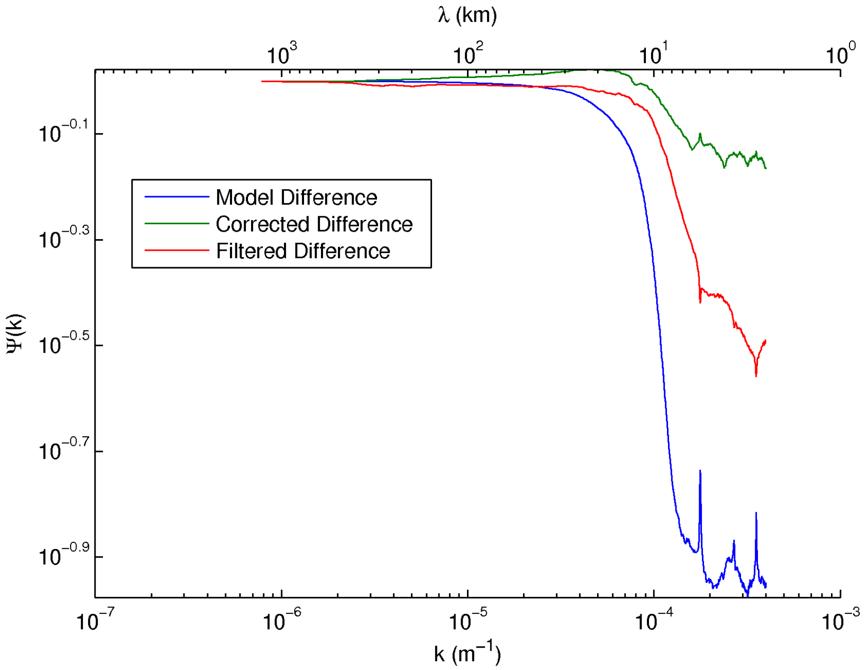

Figure 5.10: Change in spectrum between the original retrieved UHR wind field and the different changed wind fields.

5.6 Summary

There are many causes of noise and inaccuracies in ASCAT UHR wind data. Ambiguity errors are one such source that may be corrected to possibly improve the quality of these winds. A model-based approach to finding and correcting ambiguity errors has promising results. Obvious ambiguity errors are easily corrected by this approach, while areas that are difficult to model are still improved in terms of making the field more self-consistent. It also appears that the high-frequency spectral characteristics of ASCAT UHR winds are contributed to by ambiguity errors, and the corrections applied cause the spectrum to more closely approximate a $k^{-5/3}$ slope at these high spatial frequencies. A median filter also appears to benefit the high-frequency part of the spectrum, but it is unclear whether this approach brings the wind field closer to the true high-frequency wind data, or simply acts as a low-pass filter.

Chapter 6

Land Contamination Removal for ASCAT UHR Wind Retrieval

In the previous chapters, ASCAT UHR winds are analyzed, validated, and improved in terms of ambiguity selection by fitting to a data-derived model. In these processes, wind vectors near land are largely thrown out or ignored. In Chapter 3, analysis regions are chosen in the major oceans to avoid coastal areas. In Chapter 4, many of the available regions are in coastal areas, but the near-coastal wind vectors are not included in the analysis. Chapter 5 likewise does not use near-coastal winds.

In general, backscatter values over land are much higher than those over ocean water. Any ASCAT measurement over water with an SRF that is too close to land is greatly affected by the contamination of its ocean σ^0 value by leakage from the land σ^0 value. Such a measurement is said to have land contamination. Land-contaminated σ^0 values cause errors in wind retrieval, and for wind vectors to be as accurate as possible land-contaminated measurements must be excluded from the wind retrieval process [13, 26, 38].

After providing a more detailed description of land contamination in scatterometer wind retrieval, this chapter presents a method for identifying land-contaminated ASCAT σ^0 measurements and excluding them from the UHR wind retrieval process. It is based on the method proposed by Owen and Long for the $\mathrm{K_u}$-band QuikSCAT scatterometer [13] and is tuned for application to the C-band ASCAT.

6.1 Land Contamination

The σ^0 value reported for a given scatterometer measurement does not correspond to a single point. Rather, it is a weighted integral of the backscatter from the target surface over the extent of the SRF. If the surface varies spatially within that extent, the weighted average may not correspond well to the properties of the surface at the measurement center.

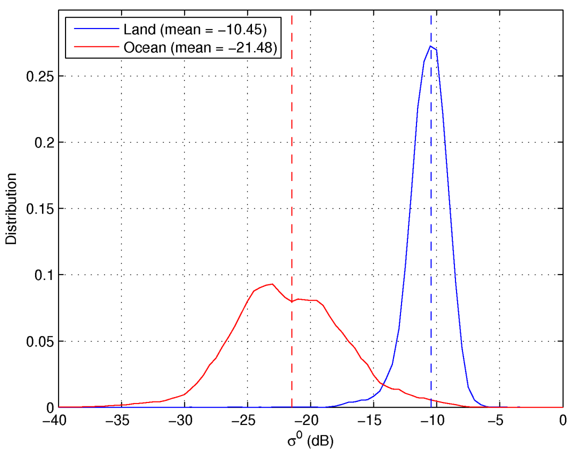

Figure 6.1: Land and ocean σ^0 distributions for a representative ASCAT SZF file with 53 000 valid land measurements and 153 000 valid ocean measurements.

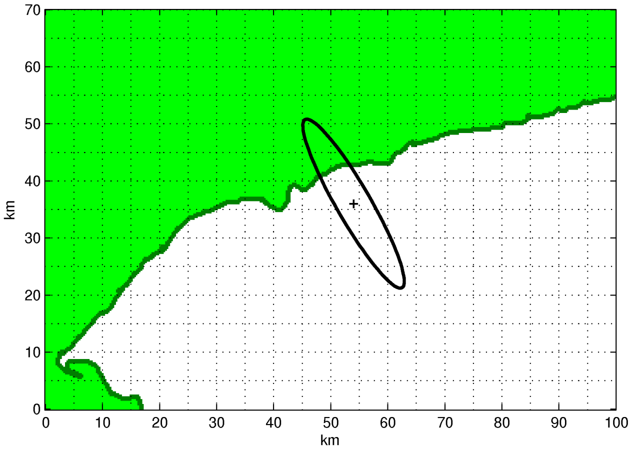

Figure 6.2: The -3 dB contour of a scatterometer measurement with an SRF that extends over land, causing contamination of the ocean σ^0 value.

This effect is very apparent in coastal locations because of the relative σ^0 values of land and ocean water.

Land typically has a much larger σ^0 value than ocean water, though the values for both can vary depending on the land or ocean surface features of a particular location. Figure 6.1 shows an example of land σ^0 and ocean σ^0 distributions for a representative ASCAT SZF file with 53 000 valid land measurements and 153 000 valid ocean measurements, excluding measurements near the coast. In this case there is an 11 dB average difference between land and ocean σ^0. With such a large difference, even if the SRF causes only a small amount of land backscatter to be averaged into the measurement, the σ^0 value may be greatly affected. This is illustrated in Figure 6.2. In this example a scatterometer measurement is shown with its center over the ocean, but with an SRF that extends partly over land. This results in land contamination, and such measurements should not be used to accurately retrieve wind vectors [13, 26].

6.2 Detecting Land Contamination

Several metrics can be used to determine the amount of land contamination for a particular scatterometer measurement. Two of these are the minimum distance to land (MDL) and the land contribution ratio (LCR) [13]. The MDL is determined by the shortest distance between either the 3-dB contour or the center of a measurement SRF and land. The LCR takes into account the full SRF to perform a weighted calculation of how much land contributes to each measurement. This is a more robust method, as it takes into account more information about each measurement. Owen and Long determined that the LCR metric has superior results for determining land contamination for QuikSCAT [13], and it is the metric that is used in this application to ASCAT.

A disadvantage of using the LCR is the need for a precise definition of the sensor SRF. If this is not available, a simpler method such as the MDL must be used. The documentation for ASCAT does not provide a detailed description of the SRF [14, 16, 39]. However, the ASCAT SRF has been estimated by Richard Lindsley [17, 40], and this estimate can be used to calculate the LCR and perform land-contamination removal for ASCAT.

The LCR is the normalized and weighted integral of the land area contributing to the backscatter for the given measurement. It is calculated as the ratio of the portion of the measurement over land and the whole measurement, assuming a constant σ^0 value over the whole surface. This can be written as

$$\text{LCR} = \frac{\sigma^0_{land}}{\sigma^0_{total}} = \frac{\iint_{A_{land}} R_{x,y}dxdy}{\iint_{A_{meas}} R_{x,y}dxdy},$$

where σ^0_{land} is the measurement land contribution, σ^0_{total} is the whole measurement, A_{land} is the area of the measurement over land, A_{meas} is the area of the whole measurement, and $R_{x,y}$ is the SRF value at location (x, y). In practice, this calculation is performed by using a discrete approximation of the SRF, in which case the equation becomes

$$\text{LCR} = \frac{\sum_{x,y} L_{x,y}R_{x,y}}{\sum_{x,y} R_{x,y}},$$

where $L_{x,y}$ is a land indicator function that is “one” for land and “zero” for ocean at location (x, y).

The relationship between LCR and σ^0 for 73 000 individual ASCAT backscatter measurements is shown in Figure 6.3 for a single representative SZF data file in the Caribbean, where there is plenty of coastal area for analysis. Figure 6.4 shows a similar plot of MDL for

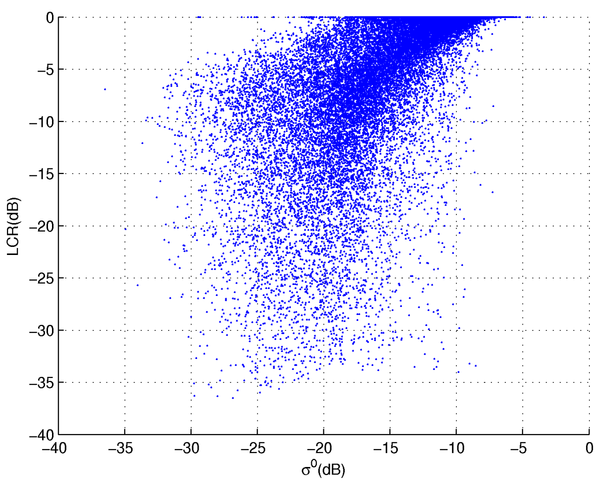

Figure 6.3: LCR versus σ^0 for representative individual ASCAT measurements in the Caribbean. At high LCR values, σ^0 increases significantly.

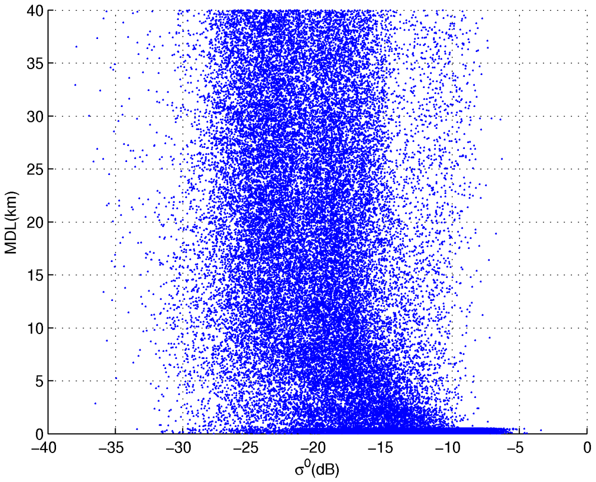

Figure 6.4: MDL versus σ^0 for representative individual ASCAT measurements in the Caribbean. At low MDL values, σ^0 increases.

comparison. As expected, σ^0 increases for both metrics when the values denote more land contribution (higher LCR, lower MDL). The correlation appears more significant for LCR, suggesting that it is the superior metric for ASCAT, as it is for QuikSCAT.

A threshold LCR value is subjectively chosen based on Figure 6.3. It appears that σ^0 begins to increase significantly above an LCR of about -10 dB. It is found that small variations in the threshold value have minimal effects on the results, and a threshold of -20 dB is chosen to be safely below the point where σ^0 increases. It is important to note that the ideal LCR threshold may vary depending on the rms wind speed in the region and other factors. However, if the threshold is chosen to be low enough, a single value will work in all situations, allowing the calculation to be more simple.

After an LCR threshold is determined, wind retrieval is performed as usual with the added step of excluding measurements that have an LCR above the chosen value of -20 dB. A wind vector can only be calculated if there are valid σ^0 values for multiple azimuth angles at the given grid locations. This means that there may be some WVCs near the coast for which a wind vector cannot be determined. However, there should be valid wind vectors closer to the coast than can be achieved without detection of land-contamination using the LCR.

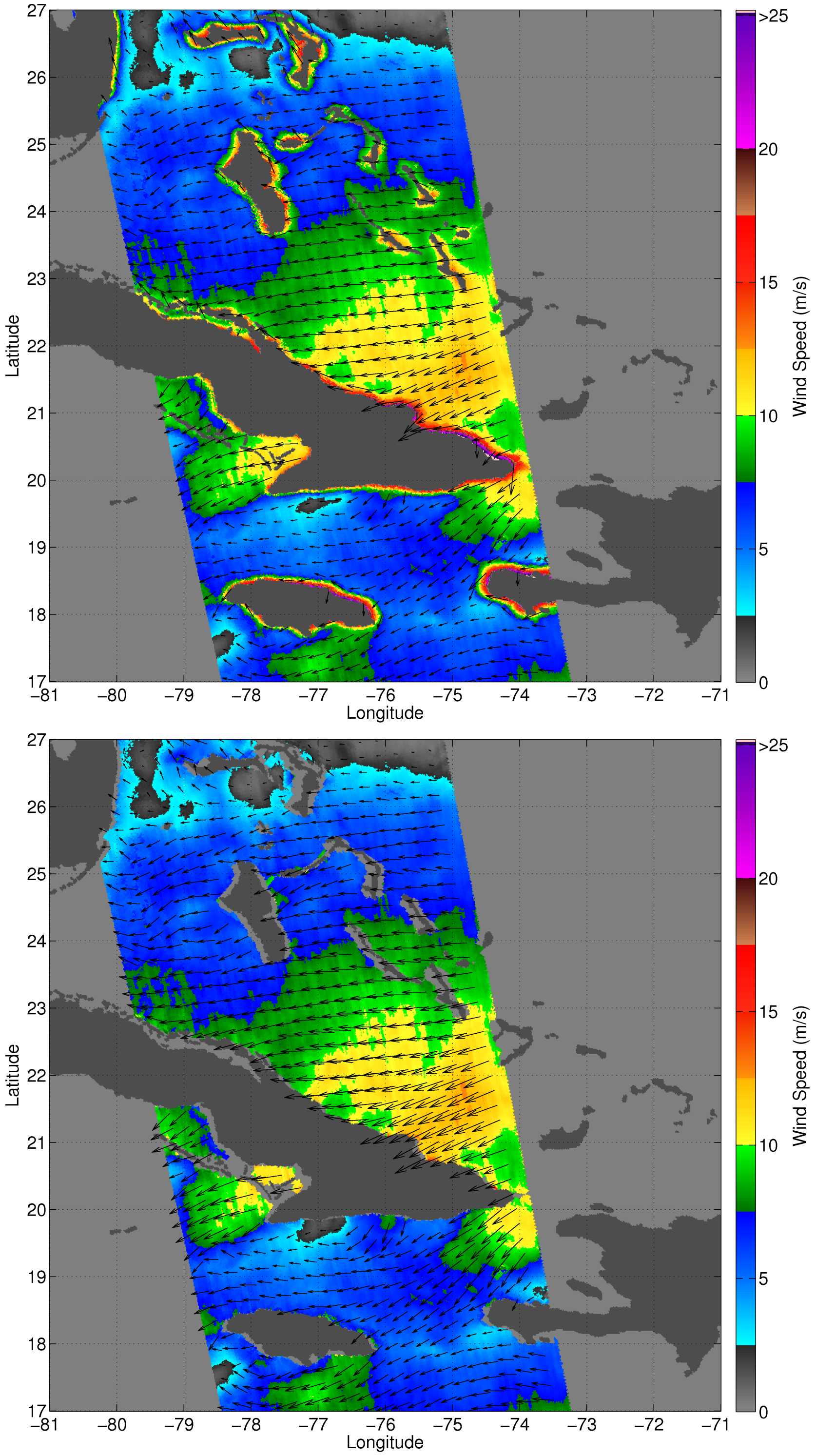

Figure 6.5: UHR winds before (top) and after (bottom) land-contamination correction. Retrieved from ASCAT on 5 Feb 2013 in the Caribbean. Direction arrows are downsampled to 0.25° spacing to increase visibility.

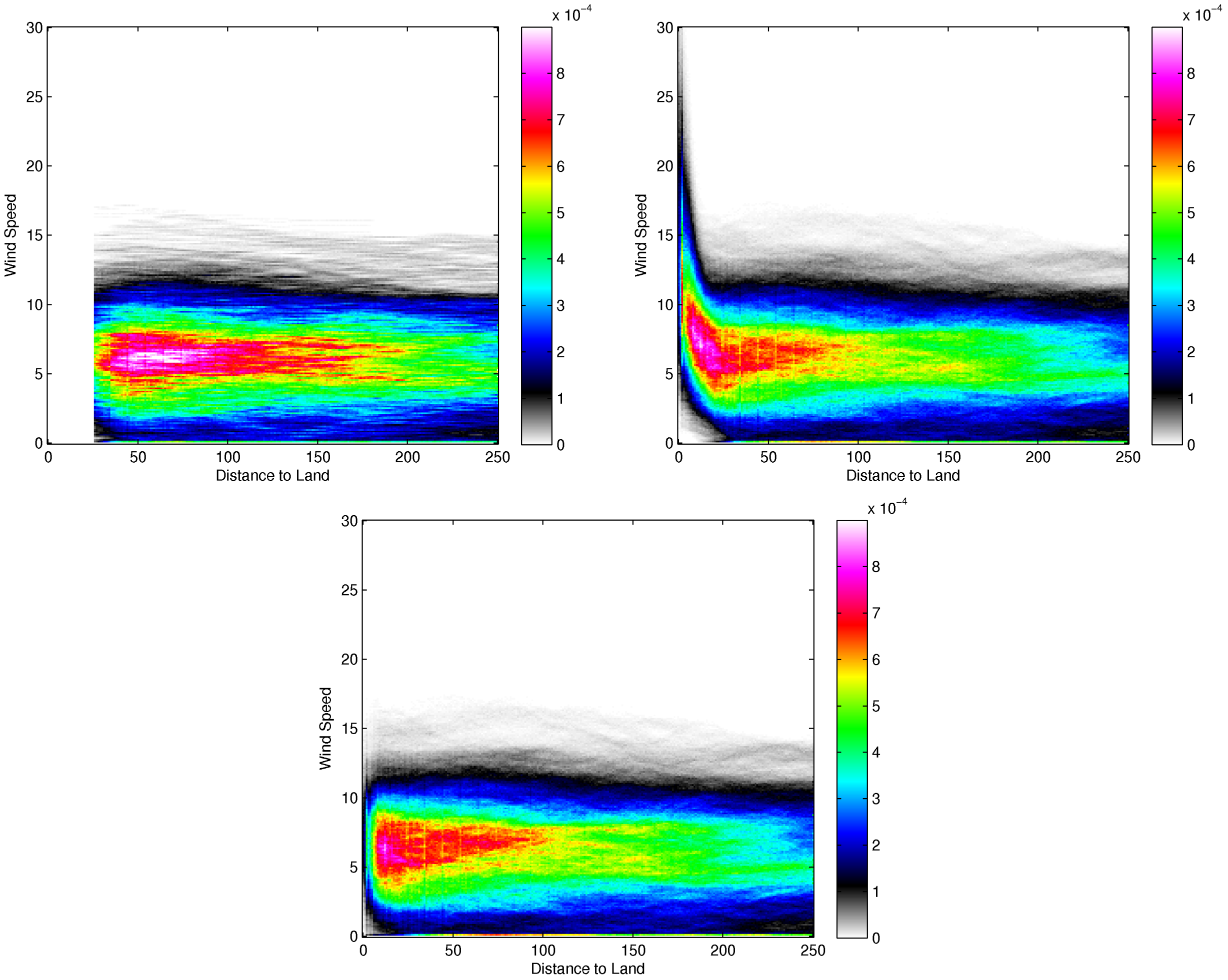

Figure 6.6: Joint distribution of wind speeds and distance to land for ASCAT L2B winds (top left), ASCAT UHR winds (top right), and LCR-corrected ASCAT UHR winds (bottom). The wind data used comes from eight days in the Caribbean in February 2013. The L2B product masks out wind vectors within 25 km of land to avoid land contamination

6.3 Results

The process described in the previous section is applied to ASCAT UHR wind retrieval, and the results are shown in Figures 6.5 to 6.7. Figure 6.5 shows a high-resolution ASCAT wind field before and after land-contamination correction. The non-corrected image shows significant land contamination near the coast, with wind speeds much greater than those in the surrounding wind field. This is typical of any scatterometer wind field that does not account for land contamination. The corrected image is greatly improved, with the near-coastal wind speeds generally matching the rest of the wind field. There are still some

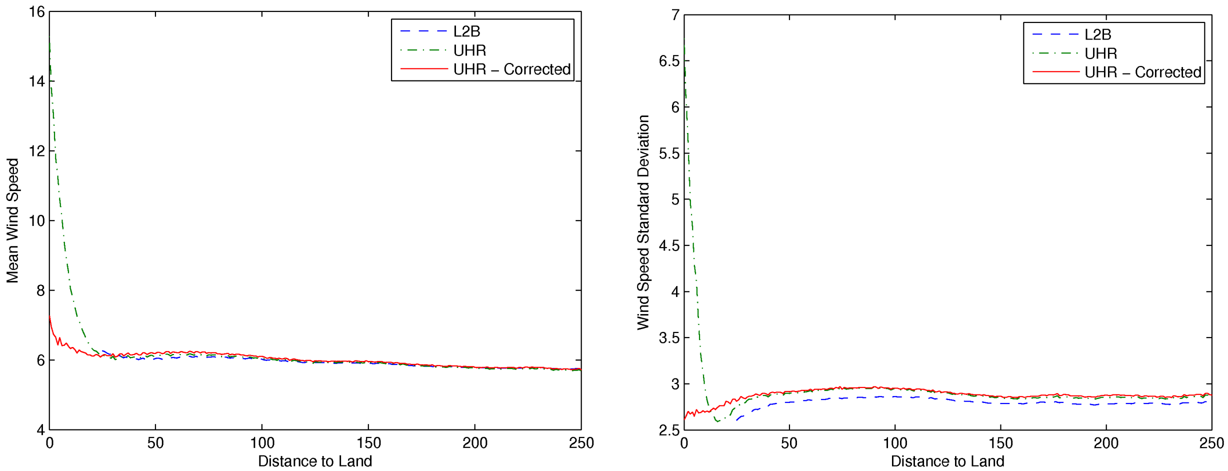

Figure 6.7: Mean (left) and standard deviation (right) of wind speed vs distance to land for ASCAT L2B, UHR, and LCR-corrected UHR winds.

spots that appear to have possible contamination, but it is small. These are likely due to modeling and estimation error in the SRF estimate [17,40]. It is also possible that there are some errors in the reported measurement locations or in the land mask.

The effect of the correction process is further illustrated by considering the variation of the wind speed distribution with distance to land [13, 26, 38]. Figure 6.6 shows this relationship for ASCAT L2B, UHR, and corrected UHR winds. The wind data used comes from eight days in the Caribbean in February 2013, where there is plenty of near-coastal area. The wind speed mean and standard deviation are shown as well in Figure 6.7. The low-resolution L2B wind data is shown for comparison. Using a conservative, fixed distance-to-land mask, the L2B wind field does not include wind vectors that are close enough to land to have any possible land contamination. Again, the wind speed is shown to increase greatly close to land for UHR wind before correction. This increase appears to begin about 25 km from the coast. After correction, the distribution appears constant across all distances, and there are still many wind vectors that are much closer than 25 km to the coast. This behavior is expected for ocean winds [13,26,38]. The mean variation plot in Figure 6.7 shows that there is still a slight increase in wind speed right next to the coast, but it is much less significant, and the standard deviation does not spike as it does before correction. This small remaining spike in the mean can likely be attributed to modeling error in the SRF estimate.

6.4 Summary

Land contamination is an important consideration in scatterometer wind retrieval, and it significantly affects near coastal ASCAT UHR winds. Retrieved ocean wind speeds increase greatly within about 25 km of land. This is readily seen in both wind field images and wind speed distributions. Land-contaminated ASCAT σ^0 measurements can be detected and excluded from wind retrieval using the LCR metric, which uses the SRF to determine how heavily a measurement is affected by contamination.

Results show that using the LCR to remove land contamination significantly improves the retrieved near-coastal wind vectors. Some of the wind vectors closest to land cannot be retrieved, but retrieval is possible much closer than the 25 km at which contamination begins. The wind speed distribution appears constant across all distances to land, although the mean wind speed plot shows there is still a slight increase at the smallest distances. This is likely due to modeling and estimation error in the SRF estimate.

Chapter 7

Conclusion

ASCAT ocean wind vectors are typically retrieved as a 25 km product on a 12.5 km grid, known as the L2B product. UHR processing allows ASCAT wind retrieval on a high-resolution 1.25 km grid. This processing method takes advantage of overlapping measurements from the scatterometer footprint. Ideally, such a high-resolution sample grid provides wind information down to a 2.5 km scale, allowing better analysis of winds with high spatial variability such as those in near-coastal regions and storms. Though the wind field is sampled on a finer grid, the actual data resolution and noise content of the underlying signal is unknown. The true resolution and quality of this UHR wind product must be validated in order to determine its usefulness and potential applications.

This thesis provides an analysis and validation of ASCAT UHR wind estimates in order to determine the improvement in resolution compared to the L2B wind product. This is done by comparing to high-resolution SAR wind estimates and by using analysis tools such as statistics, the power spectrum, and derivative fields. Improvement of the UHR wind retrieval process is also explored in order to reduce noise and increase the effective resolution. Improvement is focused on reducing ambiguity selection errors by matching to a data-derived wind field model. Lastly, a correction process is given for near-coastal wind vectors that are contaminated by land backscatter.

7.1 Summary of Results

Results suggest that UHR processing improves the data resolution of ASCAT wind estimates as compared to the standard L2B product. This improvement is difficult to quantify definitively due to a lack of adequate truth data. Evidence is given, however, that the resolution is improved by at least a factor of a factor of three (from 30 km to 10 km), and possibly a factor of seven or eight. Based on comparison to SAR winds, SAR and UHR wind fields have comparable high-resolution features that are not present in the L2B winds, validating both products. This validation has limits because of noise and lack of truth data, but the results suggest that ASCAT UHR winds are a valid high-resolution wind product that can be used with care in applications that need such additional resolution.

Visual comparison of ASCAT UHR and L2B wind fields reveals that high-resolution features appear more clearly defined in the UHR images. Contours in the UHR wind speed images are more detailed with more fine-scale variation. Also, areas of maximum or minimum wind speed are sometimes more extreme, and details of high-resolution wind events such as storms are more visible. Lastly, UHR wind processing allows wind retrieval closer to land. Additional comparison to SAR ocean winds shows comparable high-resolution features in both UHR and SAR winds that are not present or are less pronounced in L2B winds. This includes the UHR features described above. The two high-resolution products also appear to contain more noise.

A spectral comparison between UHR and L2B winds reveals that the $k^{-5/3}$ power law slope of ASCAT L2B winds is extended with UHR processing. This supports the validity of the added resolution of UHR winds. It is unclear, however, how far the spectrum should be expected to extend. At the highest wavenumbers of the UHR spectrum there appear to be two locations of deviation from the power law, which can be seen as possible noise floors. The first deviation may be contributed to by the windowing and irregular sampling in the UHR wind retrieval process, though it may represent some true wind behavior as well. The final noise floor likely shows the thermal noise and effects of undersampling. The deviation starts at about $\lambda = 10$ km while the final, noise floor occurs at about $\lambda = 4$ km. These are both a significant resolution improvement compared to the L2B noise floor which is evident at about $\lambda = 30$ km. These noise floor locations suggest a resolution improvement by a factor of 3 or improvement by a factor of 7.5 with some possible distortion due to UHR processing or noise for $\lambda < 10$ km.

Statistical comparison to SAR winds results in high correlation coefficients and low standard deviations between SAR and UHR as well as SAR and L2B. These statistics are slightly better between SAR and L2B, but very close. Such similar statistics are promising when SAR and UHR are compared on a much higher resolution grid than SAR and L2B. It gives evidence that the high resolution information of the data sets agrees just as well as the low resolution content. Higher individual standard deviations for SAR and UHR than L2B agree with the previous suggestion of more noise in these product.

Extending the spectral comparison to SAR wind speeds, the SAR spectrum has a less constant spectral slope than the UHR and L2B spectra. The SAR slope becomes more shallow at high wavenumbers, deviating significantly from $k^{-5/3}$. This causes the power levels at high wavenumbers to be much higher in the SAR wind speed spectrum than in the ASCAT spectrum, indicating more fine-scale wind variations as well as high noise content. When direction information is included by calculating the spectra of the zonal and meridional components of the wind field, the relative magnitudes of the spectra are closer. The magnitude of the UHR spectrum increases and follows a $k^{-5/3}$ slope very closely up to a 10 km resolution, while the SAR spectrum decreases slightly in magnitude and keeps a less constant spectral slope. This shows the unique benefit of UHR winds in providing high-resolution direction information. The fact that the spectral slope of the UHR winds more closely follows a constant $k^{-5/3}$ slope suggests that this product may more closely approximate the expected behavior of ocean winds at fine scales than does the SAR wind product.

An analysis of vorticity and divergence shows additional consistency between UHR and SAR wind estimates, further validating the high-resolution wind content present in the UHR product. This comparison is performed by calculating vorticity and divergence at various grid resolutions for each data set and calculating the power spectrum. The UHR results at full resolution lie between the SAR results for 3 and 4 km resolution, which is where the second noise floor in the UHR wind spectrum is located. When the vorticity and divergence are calculated at exactly the same grid resolution for UHR, L2B, and SAR winds, the spectra match very well.

The proposed improvement of the UHR wind product applies a model-based approach to finding and correcting ambiguity errors to ASCAT UHR wind data. Current UHR ambiguity selection chooses the ambiguity closest to the L2B wind vector. This works fairly well, but can be improved. Model-based correction easily finds and corrects obvious ambiguity errors, while areas that are difficult to model are still improved in terms of making the field more self-consistent. The corrections cause the spectrum to more closely approximate a $k^{-5/3}$ slope at high wavenumbers, better following the expected behavior of ocean winds.

Lastly, land-contamination correction significantly improves the performance of UHR wind retrieval near the coast. Land contamination has not previously been addressed for ASCAT UHR winds. The LCR metric is used to detect the amount of land contamination for a given σ^0 measurement and those above a certain threshold are excluded from the wind retrieval process. Some of the wind vectors closest to land cannot be retrieved, but retrieval is possible much closer than the distance of 25 km at which land contamination begins. There is still a small small amount of apparent land-contamination error, but this is likely due to modeling and estimation error in the SRF estimate.

7.2 Contributions

The previously summarized results provide specific contributions to science and engineering. The main contributions of this thesis are as follows:

1. The power spectrum is used to compare wind products and analyze their resolution content. This spectral comparison and analysis provides a unique method of validation for ocean wind data. It enables the data to be compared to expected properties of ocean winds even though there is no truth data. It allows the data be analyzed and compared according to the power levels at different spatial scales. This spectral analysis is additionally performed on the vorticity and divergence fields, allowing the benefits to be extended to derivative fields and enabling further investigation of spatial behavior and resolution.

2. Although the resolution improvement of ASCAT UHR winds cannot be precisely quantified due to a lack of truth data, the results obtained suggest improved resolution of UHR winds compared to L2B and provide quantitative values for the level of that improvement. Evidence is shown that the UHR product contains valid wind data down to at least $\lambda = 10$ km, and perhaps down to $\lambda = 3$ or 4 km with possible distortion for $\lambda < 10$ km. This is a significant improvement in either case and suggests that UHR

wind data may be useful for applications that require wind vectors on a finer scale than is typical of scatterometer winds.

3. Comparison between ASCAT UHR and ASAR wind fields provides an analysis of two high-resolution wind products that are retrieved differently using different instruments. There are issues in such a comparison, including the noise content of the data sets. The tradeoff between noise and resolution reduces the effectiveness of statistical comparison, although it can still provide useful information. Nevertheless, much is learned from comparing UHR and SAR winds, especially the presence of common fine-scale features, the similarity of their comparative statistics to that of L2B and SAR despite being compared on a finer scale, the added benefit of high-resolution direction information in UHR winds, the compatibility of the UHR product with the expected spectral properties of ocean winds, and the similarity of the derivative fields in both data sets.

4. Techniques for improving wind retrieval that have previously been applied to other scatterometer wind products are applied to the ASCAT UHR wind product. The improvement of ambiguity removal using data-derived modeling allows obvious ambiguity errors to be found and corrected and increases the self-consistency of the wind field. The removal of land contamination from near-coastal wind vectors significantly improves the UHR winds in those near-coastal areas, allowing accurate wind retrieval much closer to land and greater visibility of high-resolution wind features near the coast.

7.3 Future Work

The ASCAT UHR wind product may continue to be analyzed, validated, and improved. The methods presented in this thesis may be expanded or new methods may be explored. Some suggestions for future work include the following:

1. In Chapter 3, a brief analysis is performed of the regional variation of the ASCAT UHR wind spectrum, which suggests that the region has no visible effect on the effective resolution of the wind field. This issue can be explored further by changing the region

definitions or including additional regions. Additional regions may include equatorial, polar, or near-coastal regions.

2. Although high-resolution wind products are relatively uncommon, additional products may be found and included in the comparison besides ASAR. The Alaska SAR Demonstration Project, from which the ASAR wind product is acquired, includes some wind estimates from other SAR instruments. These include the Canadian RADARSAT SAR and the European TerraSAR-X, which are both satellite-based SAR instruments [33]. The provided winds from these different SAR instruments do not tend to overlap in time. Nevertheless, these or other high-resolution ocean winds may be investigated and compared to the results in this thesis.

3. Only one model-based ambiguity selection improvement method is explored. Other wind models or improvement methods can be investigated to judge any possible further improvement to the UHR wind product. Such methods may include spatial filters, adjusted windowing and gridding, or other wind models based on different data sets or wind parameters.

4. The land-contamination correction process may be enhanced by improving the SRF estimate used to find the LCR. Errors in land-contamination removal have been attributed to modeling and estimation error in the SRF estimate used. The model used is described in detail by Lindsley, along with its limitations and more precise models and approximations [17, 40, 41]. A more precise model is expected to improve the correction process. Such an improved SRF estimate may also improve UHR wind retrieval in general.

Bibliography

[1] F. T. Ulaby and D. G. Long, *Microwave Radar and Radiometric Remote Sensing.* Ann Arbor, MI: The University of Michigan Press, 2014. 1, 12, 15, 19, 20, 21, 37

[2] F. M. Naderi, M. H. Freilich, and D. G. Long, "Spaceborne radar measurements of wind velocity over the ocean—an overview of the NSCAT scatterometer system," *Proceedings of the IEEE*, vol. 79, no. 6, pp. 850–866, June 1991. 1, 6, 11, 13

[3] S. J. Shaffer, R. S. Dunbar, S. V. Hsiao, and D. G. Long, "A median-filter-based ambiguity removal algorithm for NSCAT," *IEEE Transactions on Geoscience and Remote Sensing*, vol. 29, no. 1, pp. 167–174, January 1991. 2, 14, 53

[4] M. H. Freilich and D. B. Chelton, "Wavenumber spectra of pacific winds measured by the Seasat scatterometer," *Journal of Physical Oceanography*, vol. 16, no. 4, pp. 741–757, April 1986. 7, 29

[5] D. G. Long and D. Luke, "The wavenumber spectra of scatterometer-derived winds," in *Proceedings of the International Geoscience and Remote Sensing Symposium*, Houston, TX, May 1992, pp. 1005–1007. 7, 29

[6] I. Van der Hoven, "Power spectrum of horizontal wind speed in the frequency range from 0.0007 to 900 cycles per hour," *Journal of Meteorology*, vol. 14, no. 2, pp. 160–164, April 1957. 7, 8, 30, 34, 35

[7] F. Said, "An evaluation of QuickSCAT UHR wind product's effectiveness in determining selected tropical cyclone characteristics," Master's thesis, Brigham Young University, 2009. 8

[8] F. M. Monaldo, D. R. Thompson, N. S. Winstead, W. G. Pichel, P. Clemente-Colón, and M. B. Christiansen, "Ocean wind field mapping from synthetic aperture radar and its application to research and applied problems," *Johns Hopkins APL Technical Digest*, vol. 26, no. 2, pp. 102–113, 2005. 8, 20, 21, 37

[9] W. G. Pichel, X. Li, F. Monaldo, C. Wackerman, C. Jackson, C. Zou, W. Zheng, K. S. Friedman, and P. Clemente-Colón, "ENVISAT ASAR applications demonstrations: Alaska SAR demonstration and Gulf of Mexico hurricane studies," in *Proceedings of the Envisat Symposium 2007*, Montreux, Switzerland, 23–27 April 2007 (ESA SP-636, July 2007). 8, 20, 38

[10] D. G. Long, "Display and computation of winds in oceanography and meteorology," BYU MERS Lab, Tech. Rep. MERS 94-001, 22 February 1994. 10

[11] W. T. Liu and X. Xie, “Measuring ocean surface wind from space,” in *Remote Sensing of the Marine Environment (Manual of Remote Sensing)*, 3rd ed., J. Gower, Ed. Amer. Soc. for Photogrammetry and Remote Sensing, 2006, vol. 6, ch. 5, pp. 149–178. 11, 16

[12] D. W. Draper and D. G. Long, “An advanced ambiguity selection algorithm for SeaWinds,” *IEEE Transactions on Geoscience and Remote Sensing*, vol. 41, no. 3, pp. 538–547, March 2003. 14, 53, 56

[13] M. P. Owen and D. G. Long, “Land-contamination compensation for QuikSCAT near-coastal wind retrieval,” *IEEE Transactions on Geoscience and Remote Sensing*, vol. 47, no. 3, pp. 839–850, March 2009. 14, 27, 64, 65, 66, 70

[14] J. Figa-Saldaña, J. J. W. Wilson, E. Attema, R. Gelsthorpe, M. R. Drinkwater, and A. Stoffelen, “The advanced scatterometer (ASCAT) on the the meteorological operational (MetOp) platform: A follow on for European wind scatterometers,” *Canadian Journal of Remote Sensing*, vol. 28, no. 3, pp. 404–412, June 2002. 17, 66

[15] European Space Agency (ESA). (2006, June) About ASCAT. Accessed: 18 Jul 2014. [Online]. Available: http://www.esa.int/Our_Activities/Observing_the_Earth/The_Living_Planet_Programme/Meteorological_missions/MetOp/About_ASCAT 17

[16] European Organisation for the Exploitation of Meteorological Satellites (EUMETSAT). (2011, August) ASCAT product guide. Accessed: 18 Jul 2014. [Online]. Available: http://oiswww.eumetsat.org/WEBOPS/eps-pg/ASCAT/ASCAT-PG-index.htm 18, 53, 66

[17] R. D. Lindsley, “Estimating the ASCAT spatial response function,” BYU MERS Lab, Tech. Rep., June 2014, unpublished. 18, 66, 70, 77

[18] European Organisation for the Exploitation of Meteorological Satellites (EUMETSAT). METOP. Accessed: 10 Feb 2014. [Online]. Available: http://www.eumetsat.int/website/home/Satellites/CurrentSatellites/Metop/index.html 18

[19] D. G. Long, P. J. Hardin, and P. T. Whiting, “Resolution enhancement of spaceborne scatterometer data,” *IEEE Transactions on Geoscience and Remote Sensing*, vol. 31, no. 3, pp. 700–715, May 1993. 19, 20, 27

[20] M. W. Spencer, C. Wu, and D. G. Long, “Improved resolution backscatter measurements with the SeaWinds pencil-beam scatterometer,” *IEEE Transactions on Geoscience and Remote Sensing*, vol. 38, no. 1, pp. 89–104, January 2000. 20, 23

[21] D. S. Early and D. G. Long, “Image reconstruction and enhanced resolution imaging from irregular samples,” *IEEE Transactions on Geoscience and Remote Sensing*, vol. 39, no. 2, pp. 291–302, February 2001. 20, 23

[22] D. G. Long, J. B. Luke, and W. Plant, “Ultra high resolution wind retrieval for SeaWinds,” in *Proceedings of the International Geoscience and Remote Sensing Symposium*, Toulouse, France, 21–25 July 2003, pp. 1264–1266. 20, 23

[23] F. M. Monaldo, D. R. Thompson, R. C. Beal, W. G. Pichel, and P. Clemente-Colón, "Comparison of SAR-derived wind speed with model predictions and ocean buoy measurements," *IEEE Transactions on Geoscience and Remote Sensing*, vol. 39, no. 12, pp. 2587–2600, December 2001. 20, 21, 37, 38, 42, 43

[24] F. M. Monaldo, D. R. Thompson, W. G. Pichel, and P. Clemente-Colón, "A systematic comparison of QuikSCAT and SAR ocean surface wind speeds," *IEEE Transactions on Geoscience and Remote Sensing*, vol. 42, no. 2, pp. 283–291, February 2004. 20, 21, 37, 38, 42, 43

[25] M. A. Richards, J. A. Scheer, and W. A. Holm, *Principles of Modern Radar*. Edison, NJ: SciTech Publishing, 2010. 21, 37

[26] A. M. Plagge, D. C. Vandemark, and D. G. Long, "Coastal validation of ultra-high resolution wind vector retrieval from QuikSCAT in the Gulf of Maine," *IEEE Geoscience and Remote Sensing Letters*, vol. 6, no. 3, pp. 413–417, July 2009. 23, 27, 64, 65, 70

[27] B. A. Williams and D. G. Long, "Estimation of hurricane winds from SeaWinds at ultra high resolution," *IEEE Transactions on Geoscience and Remote Sensing*, vol. 46, no. 10, pp. 2924–2935, October 2008. 23, 28

[28] F. Said and D. G. Long, "Effectiveness of QuikSCAT's ultra high resolution images in determining tropical storm eye location," in *Proceedings of the International Geoscience and Remote Sensing Symposium*, vol. 1, Boston, MA, 21–25 July 2008, pp. 351–354. 23, 28

[29] X. Yang, X. Li, W. G. Pichel, and Z. Li, "Comparison of ocean surface winds from ENVISAT ASAR, MetOp ASCAT scatterometer, buoy measurements, and NOGAPS model," *IEEE Transactions on Geoscience and Remote Sensing*, vol. 49, no. 12, pp. 4743–4750, December 2011. 23

[30] M. P. Owen and D. G. Long, "Towards an improved wind and rain backscatter model for ASCAT," in *Proceedings of the International Geoscience and Remote Sensing Symposium*, Honolulu, HI, 2010, pp. 2531–2534. 23

[31] Atmosphere of Earth. (2012, July) Accessed: 22 Jul 2014. [Online]. Available: http://en.wikipedia.org/wiki/Atmosphere_of_Earth 30

[32] European Space Agency (ESA). Earth online - ASAR. Accessed: 18 Jul 2014. [Online]. Available: https://earth.esa.int/web/guest/missions/esa-operational-eo-missions/envisat/instruments/asar 37, 38

[33] NOAA Center for Satellite Applications and Research (STAR). (2006, December) NOAA STAR Alaska SAR demonstration website. Accessed: 18 Jul 2014. [Online]. Available: http://www.star.nesdis.noaa.gov/sod/mecb/sar/index.html 38, 77

[34] M. A. Donelan and W. J. Plant, "A threshold for wind-wave growth," *Journal of Geophysical Research: Oceans*, vol. 114, no. C7, July 2009. 53

[35] A. E. Gonzales and D. G. Long, “An assessment of NSCAT ambiguity removal,” *Journal of Geophysical Research*, vol. 104, no. C5, pp. 11 449–11 457, May 1999. 53, 56

[36] D. G. Long, A. S. Fletcher, and D. W. Draper, “An initial SeaWinds ambiguity removal quality assessment,” in *Proceedings of the International Geoscience and Remote Sensing Symposium*, Hilton Hawaiian Village, Honolulu, Hawaii, July 2000, pp. 1036–1038. 53, 56

[37] D. G. Long, “Wind field model-based estimation of Seasat scatterometer winds,” *Journal of Geophysical Research*, vol. 98, no. C8, pp. 14 651–14 668, 15 August 1993. 56

[38] W. Tang, W. T. Liu, and B. W. Stiles, “Evaluation of high-resolution ocean surface vector winds measured by QuikSCAT scatterometer in coastal regions,” *IEEE Transactions on Geoscience and Remote Sensing*, vol. 42, no. 8, pp. 1762–1769, August 2004. 64, 70

[39] European Organisation for the Exploitation of Meteorological Satellites (EUMETSAT), *ASCAT Product Generation Function Specification*, November 2005, accessed: 26 Aug 2014. [Online]. Available: http://eumeds.eumetsat.int/groups/ops/documents/document/PDF_TEN_990009-EPS-ASCAT-PGS.pdf 66

[40] R. D. Lindsley, “Incorprating Doppler with the ASCAT spatial response function,” BYU MERS Lab, Tech. Rep., September 2014, unpublished. 66, 70, 77

[41] ——, “ASCAT SRF code,” BYU MERS Lab, Tech. Rep., June 2014, unpublished. 77

Appendix A

Undersampling vs Noise in a Power Law Spectrum

When analyzing a signal based in its power spectrum, it is important to understand how noise and sampling may affect the the shape of the spectrum. The ocean wind products studied in this thesis contain noise, but their spectrum may also be affected by the manner in which they are sampled. This appendix explores these issues for a signal that follows the power law, such as ocean winds.

A.1 Noise

Any signal generally contains noise if it is measured by some real instrument. This is an important consideration when analyzing the power spectrum of a signal that follows a power law. Such a signal has a spectrum that decreases as a constant power of frequency. If the noise is white, it does not affect the signal at low frequencies where the SNR is high, but at high frequencies a noise floor may appear as the SNR decreases due to the signal power decreasing. This is illustrated in Figure A.1 using a log-scale plot. A example of a signal that follows a power law is an ocean wind field. Ocean winds are expected to have a spatial power spectrum that approximates a $k^{-5/3}$ slope, where k is the wavenumber.

A.2 Undersampling

There is another phenomenon that may cause an apparent noise floor behavior in the power spectrum of discretely sampled ocean winds. If we assume that the $k^{-5/3}$ spectrum extends farther than the Nyquist rate, which is half the sampling rate, then the signal will be undersampled. The effect will be small because at high wavenumbers the power is very low, but an effect could still likely be seen. This is illustrated in Figure A.2 for a general decreasing spectrum. It can be seen that at high frequencies there is an "apparent noise floor" which is not really noise, but is due to the effect of aliasing.

A.3 Experiment

In order to illustrate the effects of undersampling on a signal following the power law, such as ocean winds, an ideal $k^{-5/3}$ signal is artificially generated and then undersampled. Experiments are performed by filtering the signal before sampling. This is done in an attempt to recreate some of the effects of the wind retrieval process. In this process (1) individual σ^0 measurements are a weighted integral of the true signal over some area, (2) measurements are averaged into a grid, and (3) median filtering is used in ambiguity selection. An averaging filter and a median filter are used on the original signal and the result is downsampled by

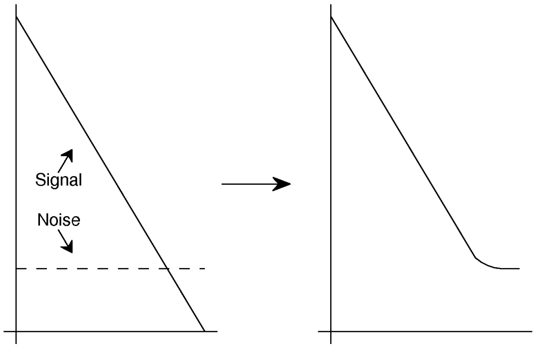

Figure A.1: Illustration of the effect of white noise on the single-sided spectrum of a signal following the power law. Axes are on a log scale.

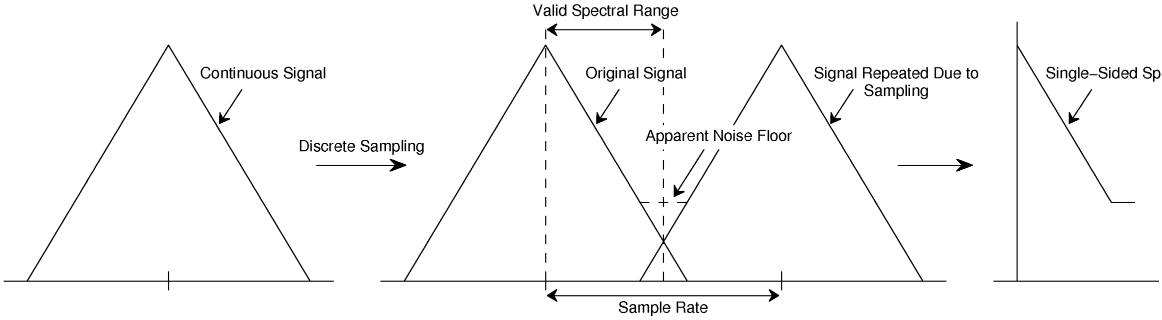

Figure A.2: Illustration of the expected effect of undersampling on a decreasing power spectrum. Sampling causes the signal to be repeated in the spectral domain. The tail of the spectrum will overlap if the spectrum extends past half the sample rate (Nyquist). This overlap will cause the signal to positively interfere and produce aliasing, which may show up as an apparent noise floor.

taking every other sample. The various spectra are shown in Figure A.3. Note that no noise is included in either the signal or the processing.

The figure demonstrates that downsampling appears to create the effect of a noise floor. Filtering before sampling reduces the power increase, but the change in shape of the spectrum tail can still be seen. This experiment illustrates that undersampling may contribute to the appearance of a noise floor in the ocean wind power spectrum at high wavenumbers.

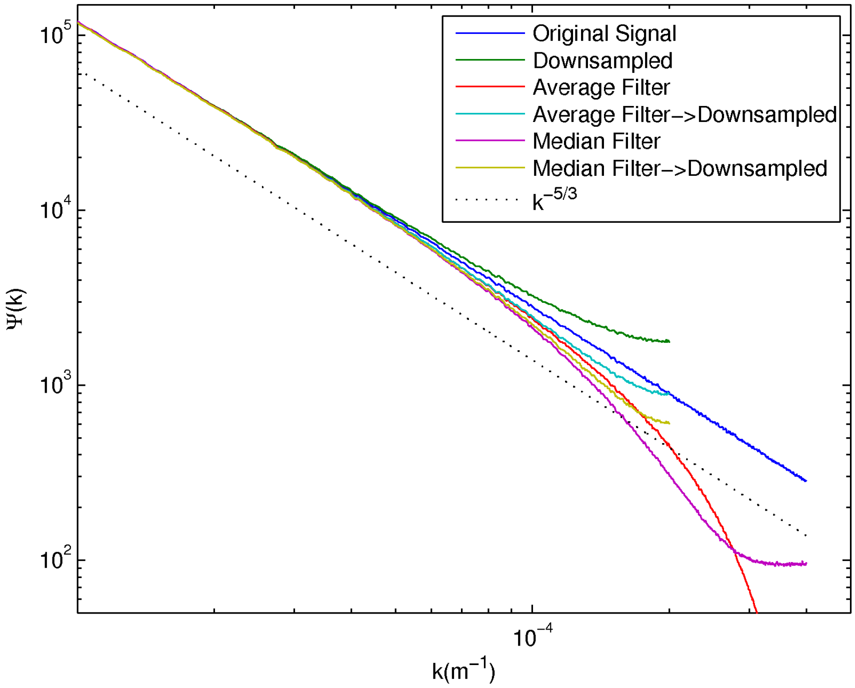

Figure A.3: A $k^{-5/3}$ signal with various forms of filtering and downsampling. The averaging filter has an impulse response that is a rect of length two, the median filter is of width three, and downsampling is performed by taking every other sample.